CHAPTER 1

INTRODUCTION

1.1 Ethylene

Ethylene, $H_2C = CH_2$, is an organic molecule containing the alkene (C=C) functional group [1]. It is produced endogeneously by plants which are the largest natural producers of ethylene. It stimulates various plant processes like fruit ripening, leaf shedding and the opening of flowers [2]. It is produced by all plant parts, including the roots, stems, flowers, leaves and fruits [3]. When plants are subjected to environmental stresses due to extreme events like floods and droughts, they will give off higher levels of ethylene. Ethylene production in plants may also be induced by other plant hormones like auxin [4]. At excessive concentrations, ethylene causes crop damage in commercial crops like the tomato plant [5]. Plants exposed to high levels of ethylene may exhibit stunted growth and leaf abortion [6]. In the agricultural industry, ethylene is used to hasten the fruit ripening process of commercial fruits like apples and bananas. However, the shelf life of other harvested crops stored in the same warehouse as the targeted

fruit will also be reduced [7]. Thus, the levels of ethylene in commercial fruits and vegetables storage warehouses must be closely monitored.

Due to the significance of ethylene in plant physiological processes, there is a demand for greater understanding of how plant growth is affected by the amount of ethylene present. While a device has been invented to monitor ethylene levels in gas samples [8], there is a need for devices which can provide more accurate detection and quantification of ethylene.

Besides natural sources, there are anthropogenic sources of ethylene. In the industry, ethylene is manufactured from steam cracking of hydrocarbons and alcohols like ethane, propane and ethanol. An example of steam cracking of ethanol is shown:

$$C_2H_5OH\ (g) \longrightarrow C_2H_4\ (g) + H_2O\ (g) \qquad (1.1)$$

The manufactured ethylene is used to synthesise many industrial products like polymers (polyethene) and refrigerants [9]. In the industry, over 60 million tonnes of polyethene is produced each year [10].

In the Earth's atmosphere, ethylene reacts readily with the hydroxyl radical and is associated with the production of ozone in the troposphere [11]. While ozone in the stratosphere shields the Earth from harmful radiation, tropospheric ozone is an air pollutant and a greenhouse gas. Tropospheric ozone is a constituent of smog, and exposure to excessive amounts of smog is linked to respiratory illnesses [12]. In addition, ethylene behaves as a greenhouse gas in the Earth's atmosphere. Incoming short-wave radiation is absorbed by ethylene, and is subsequently redirected to the Earth's atmosphere as long-wave radiation [13]. Overtime, the process results in an accumulation of energy in the atmosphere, and a warmer atmosphere is formed.

Besides the Earth's atmosphere, ethylene has been detected in other planets like Jupiter [14], Neptune [15, 16], Saturn and its satellite Titan [17]. The detection of ethylene in the atmospheres of Saturn and Titan was possible through the sending of Cassini-Huygens, an unmanned spacecraft equipped with a high resolution infrared spectrophotometer [17].

1.2 Objectives

The threats of crop damage, global warming and tropospheric ozone production associated with ethylene, coupled with the desire to investigate the atmospheric compositions of other planets, explain the need for accurate determination of the molecular structure of ethylene that will facilitate its detection and monitoring in gas samples. Thus, extensive research on ethylene and its isotopologues has been done [18-24]. Several isotopologues of ethylene have been studied in the past using high resolution Fourier transform infrared (FTIR) spectroscopy including $^{13}C_2H_3D$ [19], *trans*-$^{12}C_2H_2D_2$ [20], *cis*-$^{12}C_2H_2D_2$ [21], $^{12}C_2HD_3$ [22] and $^{12}C_2D_4$ [23]. Since the concentration of ethylene in the Earth's atmosphere is very low, accurate spectroscopic parameters are needed for the detection of ethylene in gas samples. Among the isotopologues of ethylene, very limited studies are available for the $^{13}C_2D_4$ isotopologue in the literature. In 1973, the carbon-13 frequency shifts for $^{12}C_2D_4$ in solid and gas phase were calculated by Duncan *et al.* [25]. In his work, the band centres of all vibrational bands of $^{13}C_2D_4$ were calculated and compared to the observed band centres. It was noted that the calculations provided an accurate prediction of the band centre position. For some vibrational modes, perturbation calculations were also carried out. In 2015, Tan et al. reported high resolution FTIR analysis on the ν_{12} band [24]. In their study, they derived the ground state constants up til the quartic terms of $^{13}C_2D_4$

using 985 GSCDs. They also derived the upper state constants of ν_{12} up til the quartic terms from a fit of 2079 IR transitions with a root-mean-square (rms) value of 0.00034 cm^{-1}. To date, analyses on the other vibrational bands like ν_9 have not been reported.

In order to have a better understanding of the molecular structure of $^{12}C_2H_4$, it is necessary to analyse the spectrum of other ethylene isotopologues like $^{13}C_2D_4$ [26]. Isotopic substitution is needed to understand how molecular rotations and vibrations are affected by molecular mass. When the rotational constants of substituted ethylene are compared to those of unsubstituted ethylene, a better understanding of bond lengths and bond angles can be achieved [27]. Therefore, this project aims to study the ν_9 band of the $^{13}C_2D_4$ isotopologue. The ν_9 mode, which corresponds to C-D stretching, is one of the 12 vibrational modes of $^{13}C_2D_4$ [28]. In particular, this work aims to derive accurate values of the ro-vibrational constants of the ν_9 band of $^{13}C_2D_4$. Knowing the values of the ro-vibrational constants will lead to greater understanding of the molecular structure of ethylene. Parameters that describe the ro-vibrational structure include the molecular geometry and vibration-rotation interaction parameters [29].

1.3 Overview

The general outline of this thesis includes the following:

Chapter 1 is about the description of the ethylene molecule and the significance of ethylene gas in biological and atmospheric processes. The objectives of the project are also covered in this chapter.

In chapter 2, the theoretical background of molecular spectroscopy is discussed. The applications of different types of spectroscopy like microwave spectroscopy and radiowave spectroscopy is outlined in chapter 2. An overview of the different classifications of molecules according to molecular spectroscopy, namely linear molecules, symmetric tops, spherical tops and asymmetric tops is included as well. Besides, concepts about molecular symmetry are introduced to explain the types of spectral band that can be produced.

In chapter 3, the mathematics of FTIR spectroscopy is discussed. The chapter also explains the relevance of apodisation and digitization in spectroscopy. Factors affecting spectral resolution and the advantages of FTIR spectroscopy are discussed as well.

Experimental details like the instrumental setup, source, input system, optical system and analytical software used are presented in chapter 4. Subsequently, the experimental procedures carried out are described. The chapter also includes a description of how calibration was carried out.

In chapter 5, the process of spectral analysis is discussed. A table of ground state and upper state constants obtained from this work is also shown.

The report ends with concluding remarks in chapter 6. The motivation of the project is reiterated and a summary of the results obtained is discussed.

Appendix A lists the combination differences used in the analysis to get the ground state constants, while appendix B lists the spectral lines used to fit the upper state constants.

CHAPTER 2

THEORY OF MOLECULAR SPECTROSCOPY

2.1 Electromagnetic Spectrum

Electromagnetic (EM) waves are a result of electric and magnetic fields oscillating in phase with each other, with the oscillatory plane of electric field perpendicular to the oscillatory plane of magnetic field. EM waves are transverse waves. In vacuum, the EM waves propagate at a speed of 3.00×10^8 m s^{-1}. In the EM spectrum, the EM waves are classified by wavelength. The EM spectrum is illustrated in Table 2.1.

Table 2.1 *Types of EM waves and their corresponding wavelengths*

Region	Wavelength (m)
Radiowave	10^{-1}
Microwave	10^{-2}
Infrared	10^{-5} to 10^{-4}
Visible	10^{-7}
X-ray	10^{-9}
Gamma ray	10^{-11}

Different types of EM waves correspond to different types of atomic and molecular processes. Radiowaves correspond to changes in electron spin and nuclear spin, microwaves correspond to transitions between rotational energy levels, infrared waves correspond to transitions between vibrational levels, visible waves and X-rays correspond to changes in electron distributions and gamma rays correspond to changes in nuclear configurations. [1]

2.2 Molecular Absorption of Electromagnetic Radiation

EM radiation is absorbed when the net electric dipole moment of a molecule interacts with the fluctuating component of the electric field present in EM waves. Molecules have a net electric dipole moment if there is an uneven distribution of electron density in the molecule. Mathematically, in a heteronuclear molecule with a permanent net positive charge $+q$ and a permanent net negative charge $-q$, the electric dipole moment, μ_p, is calculated using the equation

$$\mu_p = qr \tag{2.1}$$

where r is the bond length between atoms.

The net electric dipole moment of a heteromolecule oscillates in the presence of a fluctuating electric field. In the process, energy from EM radiation is absorbed and emitted when the molecule transits between energy states [30]. The oscillating dipole moment is a result of molecular rotation, and the process is illustrated in Figure 2.1 [31].

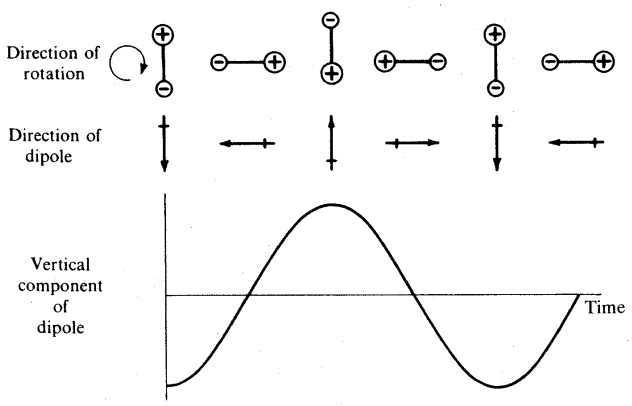

Figure 2.1 *Oscillating dipole moment as a result of molecular rotation*

Unlike heteronuclear molecules, homonuclear molecules like Cl_2 and H_2 do not have a dipole moment. Thus, the rotations of homonuclear molecules do not interact with EM radiation.

Besides rotations, molecular vibrations can also produce a fluctuating electric dipole moment, depending on whether the vibration is symmetric or asymmetric. For example, the carbon dioxide, CO_2 molecule, has a partial positive charge on the carbon atom and partial negative charges on the oxygen atoms. However, the individual dipole moments along the C-O bonds cancel out, and thus CO_2 is a molecule without a net dipole moment. When the molecule

undergoes symmetric stretching, at any point in time, both C-O bonds are stretched or compressed by the same extent. Throughout the stretching process, the net dipole moment remains zero, and there is no interaction between the molecular vibration and EM radiation. The symmetric stretching process is illustrated in Figure 2.2 [31].

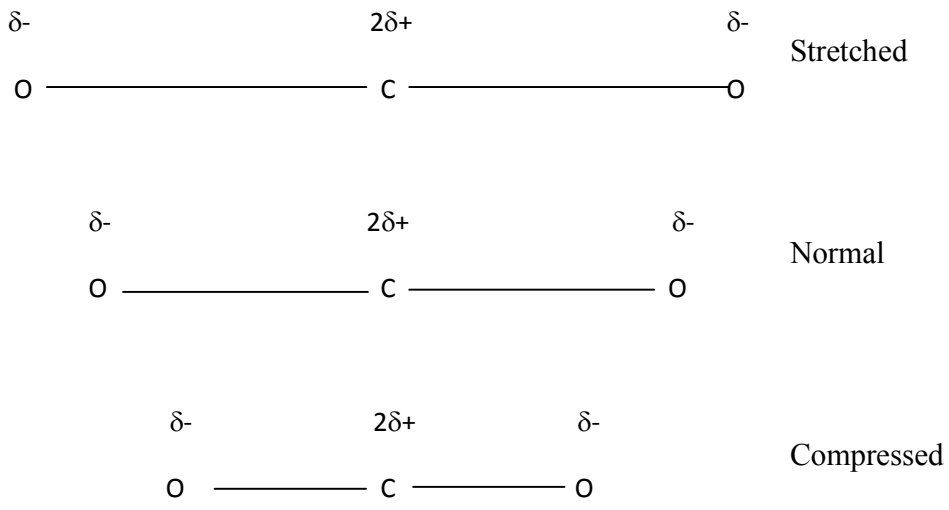

Figure 2.2 *Symmetric stretching of CO_2 molecule*

On the other hand, when the CO_2 molecule undergoes asymmetric stretching, one C-O bond is compressed and the other C-O bond is stretched. Through asymmetric stretching, a net electric dipole moment is generated. The net electric dipole moment interacts with EM radiation by oscillating in response to the fluctuating electric field. The molecule absorbs EM radiation and a spectrum is produced. The asymmetric stretching process is illustrated in Figure 2.3 [31].

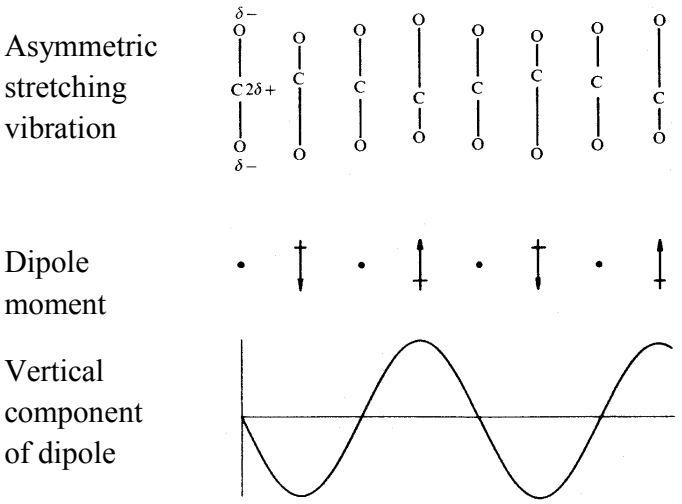

Figure 2.3 *Asymmetric stretching of CO_2 molecule*

Besides asymmetric stretching, a fluctuating dipole moment can be produced due to bending.

The bending process is illustrated in Figure 2.4 [31].

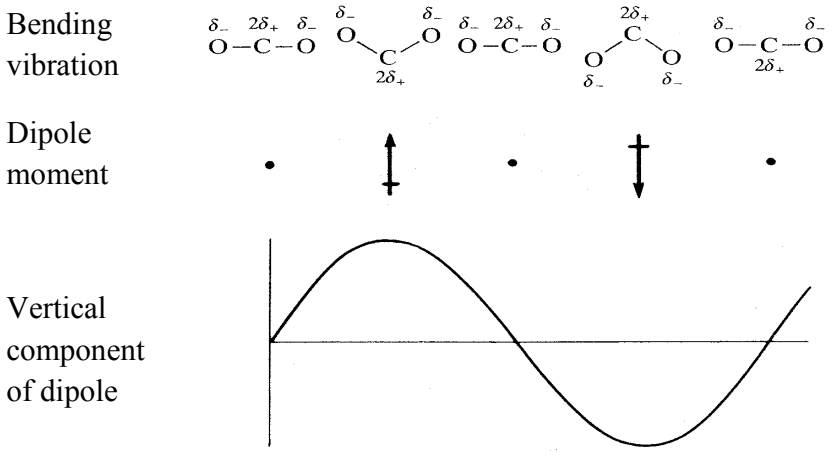

Figure 2.4 *Bending of CO_2 molecule*

It is important to note that the above illustrations have greatly exaggerated the amplitude of molecular vibrations. In reality, the maximum amplitude of molecular vibrations is about 10^{-10} m [31].

The energy states of a molecule are quantised, and the frequencies of EM radiation that are absorbed will also be quantised. Thus, the transmission spectrum will record discrete spectral peaks rather than a continuous spectrum. The frequencies of radiation that are absorbed by the molecule, ν, satisfy the following equation

$$E = h\,\nu \tag{2.2}$$

where h is the Planck's constant and E is the energy difference between the final energy state and the initial energy state.

Since the project aims to study the ro-vibrational structures of the ethylene molecule, it involves the collection of a spectrum in the mid infrared range. Mid infrared waves have wavenumbers ranging from 400 cm^{-1} to 4000 cm^{-1}.

2.3 Moments of Inertia

The moment of inertia, I, of a rotating body about a given axis is defined as

$$I = \sum m_i\, d_i^2 \tag{2.3}$$

where d_i is the perpendicular distance of the mass element m_i from the axis. The moment of inertia describes a rotating body's resistance to rotational acceleration. A higher I value means a greater resistance to rotational acceleration. For a given molecule, there are three mutually

perpendicular principal axes of rotation, the *A* axis, *B* axis and *C* axis, each corresponding to a principal moment of inertia, I_A, I_B and I_C respectively. By convention,

$$I_A \leq I_B \leq I_C \tag{2.4}$$

The components of angular momentum, P_a, P_b and P_c about the *A* axis, *B* axis and *C* axis respectively can be calculated from the following equations

$$P_a = I_a \omega_a \tag{2.5}$$

$$P_b = I_b \omega_b \tag{2.6}$$

$$P_c = I_c \omega_c \tag{2.7}$$

where ω is the angular velocity.

In general, the rotational energy is given by the following equation

$$E = \frac{P_A^2}{2I_A} + \frac{P_B^2}{2I_B} + \frac{P_C^2}{2I_C} \tag{2.8}$$

2.4 Molecular Classification

In molecular spectroscopy, molecules are classified according to the relative values of I_A, I_B and I_C.

2.4.1 Linear Molecules

In linear molecules, the atoms are arranged in a straight line. I_A, which is the moment of inertia along the bond axis, is approximately zero, while $I_B = I_C$. Examples of linear molecules are CO_2 and O_2.

The rotational energy E_r of a molecule is quantized. For the linear molecule, E_r is given by

$$E_r = \frac{h^2}{8\pi^2 I_B} J(J+1) \text{ Joules} \tag{2.9}$$

J is the rotational quantum number, and can only take integer values from zero onwards.

Rotation is about any axis through the centre of mass and at right angles to the internuclear axis [30]. For a given diatomic molecule, the rotational energy is only dependent on one quantum number, J. Thus, the quantum number J is sufficient to describe the state of a diatomic molecule. The collected spectrum is a graph of intensity against wavenumber, and E_r is reexpressed in terms of wavenumber ε_J for convenience. ε_J is given by

$$\varepsilon_J = \frac{E_J}{hc} = \frac{h}{8\pi^2 I_B c} J(J+1) cm^{-1} \tag{2.10}$$

By defining $B = \frac{h}{8\pi^2 I_B c} cm^{-1}$ as the rotational constant for rotation about the B axis, ε_J is reexpressed as

$$\varepsilon_J = BJ\,(J+1)\ cm^{-1} \tag{2.11}$$

Thus, the wavenumber difference between a state J and a state J+1 is

$$\Delta\nu = 2B\,(J+1)\ cm^{-1} \tag{2.12}$$

Given the selection rule

$$\Delta J = \pm 1 \tag{2.13}$$

for a rigid diatomic molecule, it is predicted that the spectral lines observed will be evenly spaced with a spacing of $2B$ cm^{-1}.

However, additional terms in the expression for rotational energy are required to account for the change in energy due to centrifugal distortion. [26] Centrifugal distortion is a result of the non-rigidity of molecule. When the molecule rotates and vibrates, the bond length changes with time. As J increases, the separation distance between atoms increases and the actual rotational energy is reduced. Thus, the corrected energy values are given by the formula

$$E_J = h\,(BJ\,(J+1)-DJ^2(J+1)^2) \tag{2.14}$$

with $D = \frac{4B^3}{\omega^2}$ for diatomic molecules.

In general, B is dependent on the vibrational energy state of the molecule. For a diatomic molecule, B_v for a given energy state v is given by

$$B_v = B_e - \alpha(v + \tfrac{1}{2}) \tag{2.15}$$

where B_e is the equilibrium value of B and α is the vibration-rotation interaction constant.

2.4.2 Symmetric tops

Molecules with two equal principal moments of inertia are known as symmetric tops. Symmetric tops are further classified into prolate symmetric tops and oblate symmetric tops. When

$$I_B = I_C > I_A \tag{2.16}$$

the molecule is a prolate symmetric top and when

$$I_A = I_B < I_C \tag{2.17}$$

the molecule is an oblate symmetric top. An example of a prolate symmetric top is ammonia, while an example of an oblate symmetric top is benzene. A geometrical illustration of the mass distribution of a prolate top and an oblate top is shown in Figure 2.5.

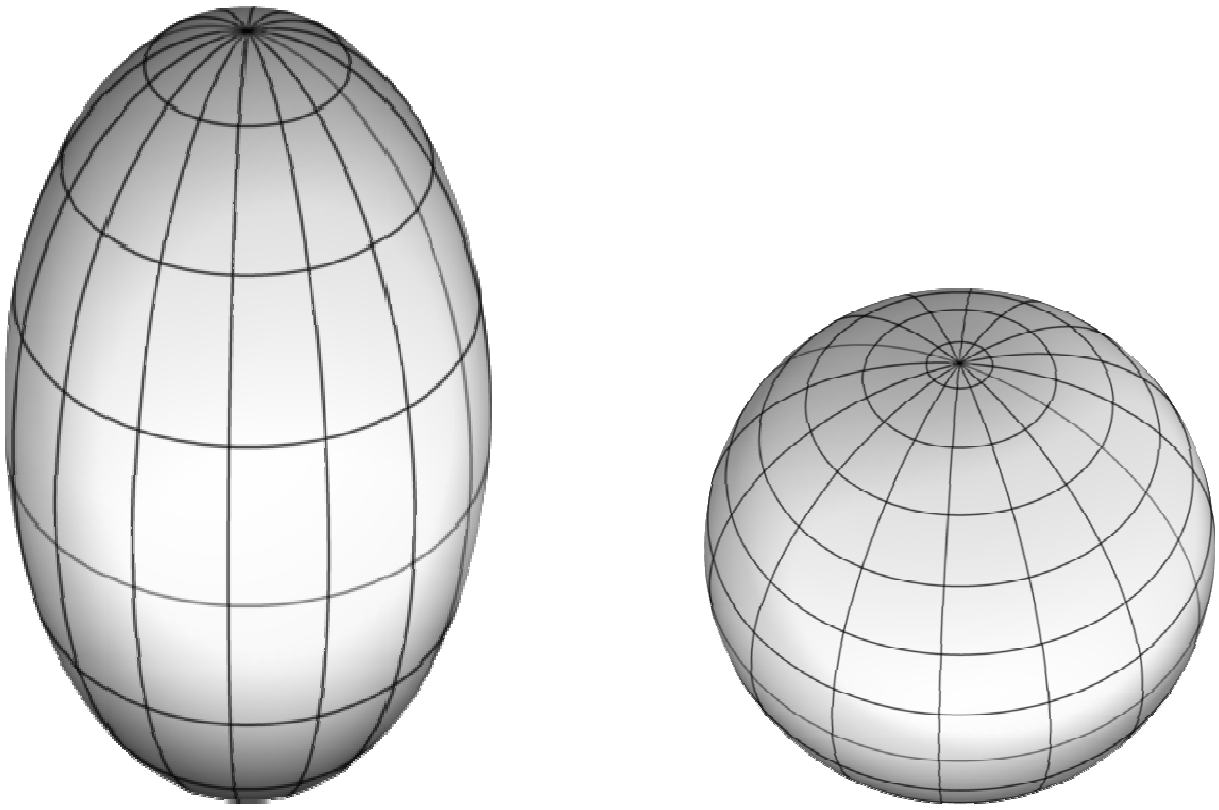

(a) (b)

Figure 2.5 *(a) Geometrical illustration of prolate top (b) Geometrical illustration of oblate top*

The molecular structures of ammonia and benzene are shown in Figure 2.6.

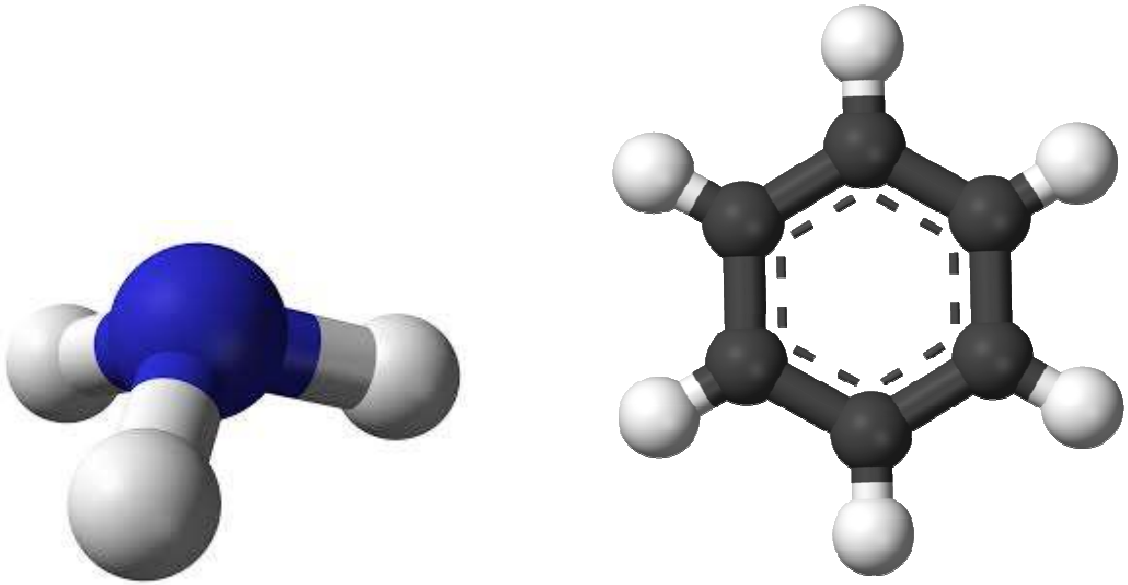

(a) (b)

Figure 2.6 *(a) Ammonia (prolate top) (b) Benzene (oblate top)*

Unlike linear molecules, symmetric tops rotate about any axis through the centre of mass, and the rotational axis is not necessarily at right angles to the internuclear axis [30]. The rotational energy, ε_J, is determined by two quantum numbers, J and K.

For a prolate symmetric top,

$$\varepsilon_J = BJ(J+1) + (A-B)\,K^2 \tag{2.18}$$

For an oblate symmetric top,

$$\varepsilon_J = BJ(J+1) + (C-B)\,K^2 \tag{2.19}$$

A, B and C are related to I_A, I_B and I_C respectively in the following way

$$A = \frac{h}{8\pi^2 I_A c} cm^{-1} \tag{2.20}$$

$$B = \frac{h}{8\pi^2 I_B c} cm^{-1} \tag{2.21}$$

$$C = \frac{h}{8\pi^2 I_C c} cm^{-1} \tag{2.22}$$

In both cases, the value of angular momentum component along the unique axis is given by $K\hbar$. Figure 2.3 [31] illustrates the energy levels for a prolate symmetric top and an oblate symmetric top.

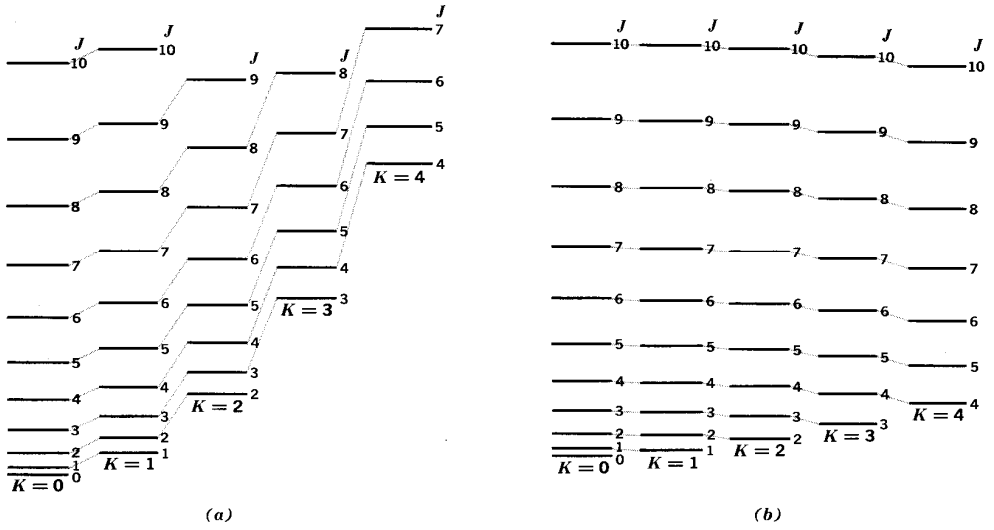

Figure 2.7 *Energy level diagram for (a) prolate symmetric top and (b) oblate symmetric top*

As shown in Figure 2.7, for a given J value, the energy increases for the prolate symmetric top and decreases for the oblate symmetric top with increasing K.

Accounting for the effects of centrifugal distortion, the rotational energies of a given state with quantum numbers J and K are given by

$$\varepsilon_{J,K} = BJ(J+1) + (A-B)K^2 - D_J J^2 (J+1)^2 - D_{JK} J(J+1)K^2 - D_K K^4 \tag{2.23}$$

where D_J, D_{JK} and D_K are the centrifugal distortion constants.

2.4.3 Spherical tops

When a molecule has all three moments of inertia identical, such that

$$I_A = I_B = I_C \tag{2.24}$$

it is known as a spherical top. An example of a spherical top is the methane molecule, as shown in Figure 2.8.

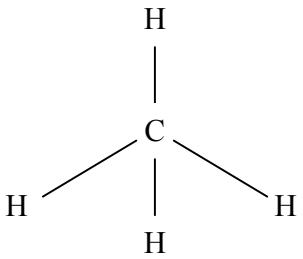

Figure 2.8 *Structure of methane*

Due to their molecular symmetry, there is no net dipole moment and rotation alone will not give a net fluctuating dipole moment.

2.4.4 Asymmetric tops

The last class of molecules is known as asymmetric tops, where

$$I_A \neq I_B \neq I_C \tag{2.25}$$

The $^{13}C_2D_4$ molecule studied in the project is an example of an asymmetric top. The structure of the $^{13}C_2D_4$ molecule is illustrated in Figure 2.9.

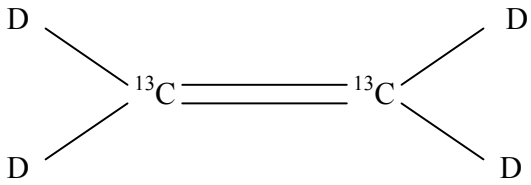

Figure 2.9 *Structure of $^{13}C_2D_4$ molecule*

The degree of asymmetry is quantified by the asymmetry parameter

$$\kappa = \frac{2B - A - C}{A - C} \tag{2.26}$$

where A, B and C are the rotational constants along the A axis, B axis and C axis respectively. κ has values ranging from -1 for a prolate symmetric top to +1 for an oblate symmetric top. For the $^{13}C_2D_4$ molecule, κ = -0.83 approximately. Thus, $^{13}C_2D_4$ is classified as a near prolate molecule.

The cylindrical tensor has been proposed by Papousek and Aliev [27] to express the rigid rotor Hamiltonian, H_r, for the asymmetric top molecule as given in the equation below,

$$H_r = \frac{1}{2}(B_x + B_y)J^2 + (B_z - \frac{1}{2}(B_x + B_y))J_z^2 + \frac{1}{4}(B_x - B_y)(J_+^2 + J_-^2) \tag{2.27}$$

where B_x, B_y and B_z are the rotational constants and are calculated from the principal moments of inertia, I_x, I_y and I_z

$$B_x = \frac{h}{8\pi^2 cI_x}; B_y = \frac{h}{8\pi^2 cI_y}; B_z = \frac{h}{8\pi^2 cI_z} \tag{2.28}$$

where h is the Planck's constant while c is the speed of light.

$$J^2 = J_x^2 + J_y^2 + J_z^2 \tag{2.29}$$

where J_x, J_y and J_z are the components of angular momentum along the principal axes.

J_+ and J_- are known as the raising and lowering operators, and are constructed in the following way

$$J_+ = J_x + iJ_y \tag{2.30}$$

$$J_- = J_x - iJ_y \tag{2.31}$$

The eigenvalue equations associated with J_+ and J_- are

$$J_+ | J,K > = \sqrt{j(j+1) - k(k+1)} \, | J,K+1 > \tag{2.32}$$

$$J_- | J,K > = \sqrt{j(j+1) - k(k-1)} \, | J,K-1 > \tag{2.33}$$

Due to the existence of the raising and lowering operator in the Hamiltonian operator, the Hamiltonian is no longer diagonal with respect to the $| J, K >$ basis. Thus, it is necessary to introduce a new set of basis which will block diagonalise the Hamiltonian [32]

$$| J,K^+ > = \frac{1}{\sqrt{2}}(- | J,K > + | J,-K >) \tag{2.34}$$

$$| J,K^- > = \frac{1}{\sqrt{2}}(| J,K > + | J,-K >) \tag{2.35}$$

Besides, while J is a quantum number that is used to specify the rotational state, the angular momentum component along any direction is no longer constant and cannot be used to

specify the rotational state of an asymmetric top [30]. The integer quantity, τ, is introduced to label the $2J+1$ states for a given value of J, with

$$-J \leq \tau \leq +J \tag{2.36}$$

τ is calculated by introducing the quantum numbers K_a and K_c

$$\tau = K_a - K_c \tag{2.37}$$

K_a and K_c are quantum numbers used to calculate the allowed energy values, ε_J, in the limiting cases of the prolate symmetric top and the oblate symmetric top respectively.

$$\varepsilon_J = BJ(J+1) + (A-B) K_a^2 \tag{2.38}$$

$$\varepsilon_J = BJ(J+1) + (C-B) K_c^2 \tag{2.39}$$

In an asymmetric top, the rotational energy levels are described by the quantum numbers J, K_a and K_c. Since K_a and K_c are associated with the components of angular momentum along the A axis and C axis respectively, either $K_a + K_c = J$ or $K_a + K_c = J+1$.

Practically, it is difficult to calculate the rotational energy levels of asymmetric tops. However, equations have been developed to calculate the rotational energy levels of slightly asymmetric tops. Neglecting centrifugal distortion, the energy levels for a prolate near-symmetric rotor [33] is expressed as

$$\varepsilon_J = \frac{1}{2}(B+C)J(J+1) + \left[A - \frac{1}{2}(B+C)\right] W(b_p) \tag{2.40}$$

where $W(b_p)$ is calculated from the following equation:

$$W(b_p) = K_a^2 + c_1 b_p + c_2 b_p^2 + \ldots \tag{2.41}$$

b_p is the asymmetry parameter used for a prolate near-symmetric rotor and is given by

$$b_p = (C - B)/(2A - B - C) \tag{2.42}$$

The energy levels for an oblate near-symmetric rotor [33] is expressed as

$$\varepsilon_J = \frac{1}{2}(A + B)J(J+1) + \left[C - \frac{1}{2}(A + B)\right]W(b_o) \tag{2.43}$$

where $W(b_p)$ is calculated from the following equation:

$$W(b_o) = K_c^2 + c_1 b_o + c_2 b_o^2 + \ldots \tag{2.44}$$

b_o is the asymmetry parameter used for an oblate near-symmetric rotor and is given by

$$b_o = (A - B)/(2C - B - A) \tag{2.45}$$

2.5 Molecular Vibrations

Linear molecules have 3*N*-5 vibrational degrees of freedom, while non-linear molecules have 3*N*-6 vibrational degrees of freedom, where *N* is the number of atoms in a molecule [34]. In the case of the ethylene molecule (*N*=6), there are a total of 12 different vibrational modes. Each mode corresponds to a given vibrational motion. The vibrational motions of molecules of X_2Y_4 type, like $^{12}C_2H_4$ and $^{13}C_2D_4$ are illustrated in Figure 2.10.

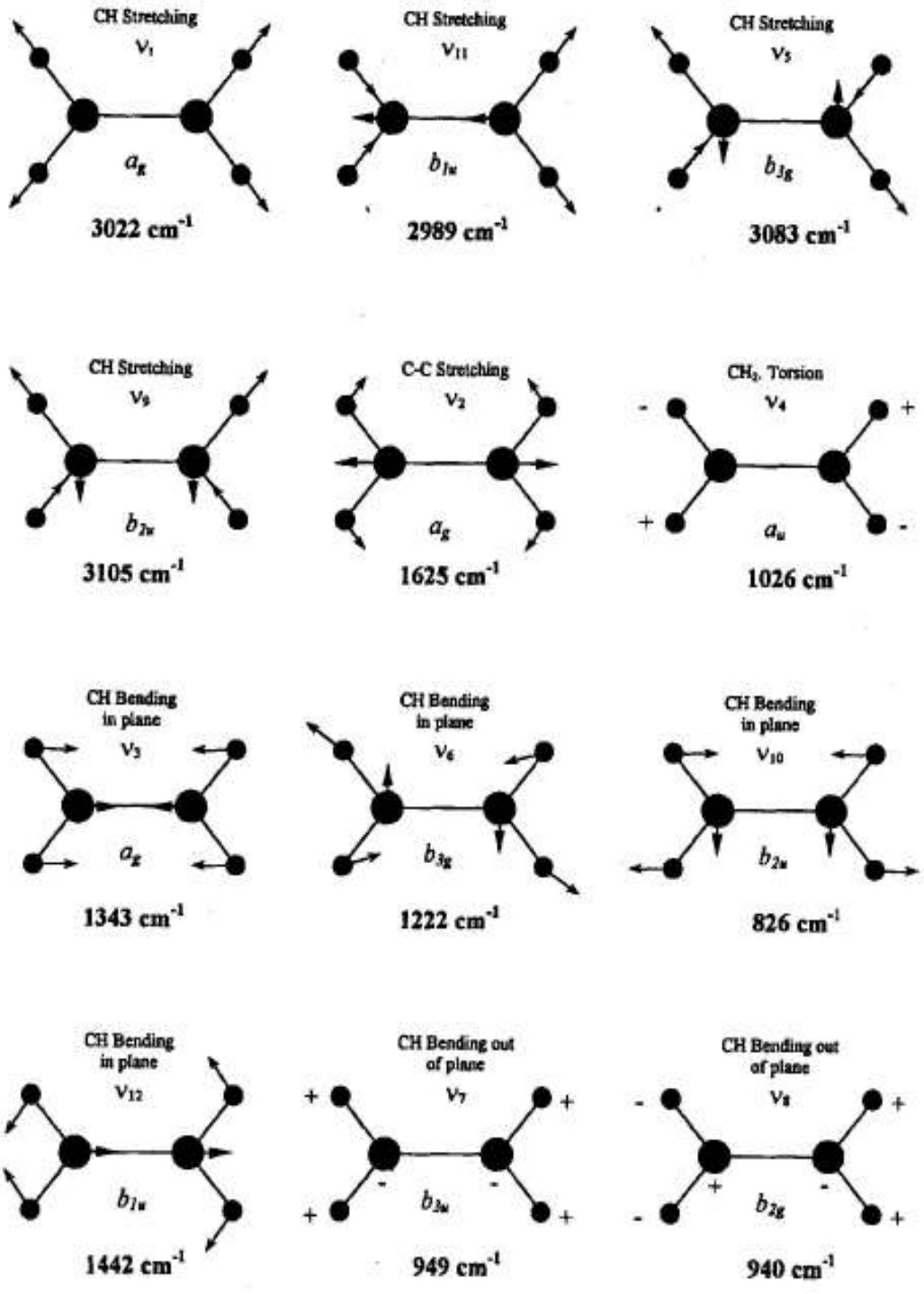

Figure 2.10 *Vibrational modes of the $^{12}C_2H_4$ ethylene molecule* [29]

As shown in Figure 2.10, the v_9 band studied in the project corresponds to C-D stretching. Even though the $^{13}C_2D_4$ does not have a net dipole moment, it is still possible to obtain an infrared spectrum. This is because during asymmetric stretching or bending, a net dipole moment is generated. The net dipole moment interacts with incident radiation and energy can be absorbed or emitted, giving rise to a spectrum.

However, not all vibrational modes of $^{13}C_2D_4$ will give a spectrum. For example, the v_4 band, corresponding to CH_2 torsion, does not give a spectrum. This is because CH_2 torsion does not generate a net dipole moment.

As shown in Figure 2.5, each vibrational mode is associated with a type of symmetry (A_g, A_u, B_{1g}, B_{1u}, B_{2u}, B_{3u}). Symmetry is used to explain why some transitions are allowed and why some transitions are forbidden [35]. Mathematically, for a transition to be allowed, the transition dipole moment integral in the volume $d\tau$ must be non-zero:

$$\int_{-\infty}^{\infty} \psi_1 \mu \psi_0 d\tau \neq 0 \tag{2.46}$$

ψ_1 and ψ_0 are the excited state and ground state wavefunctions respectively, while μ is the dipole moment operator. To have a non-zero transition dipole moment integral, $\psi_1 \mu \psi_0$ must be totally symmetric.

For a band to be infrared active, the ground state and the upper state must have different indexes "*u*" and "*g*". The different indexes *u* and *g* are only applicable to molecules with a centre of symmetry [36]. In $^{13}C_2D_4$, the centre of symmetry is the midpoint of the C=C bond. When all the atoms of $^{13}C_2D_4$ are reflected about the centre of symmetry, the molecule remains invariant. Given that the ground state has symmetry A_g, transitions to vibrational states having the same

index *g* are forbidden by symmetry. Transition to the vibrational state of A_u type is also forbidden [35]. Thus, the ν_1, ν_2, ν_3, ν_5, ν_6 and ν_8 bands are infrared inactive, while the ν_7, ν_9, ν_{10}, ν_{11} and ν_{12} bands are infrared active.

By treating the vibrating molecule as a simple harmonic oscillator, the oscillatory frequency, ν, is expressed as

$$\nu = \frac{1}{2\pi}\sqrt{\frac{k}{\mu}} \tag{2.47}$$

where μ is the reduced mass and k is the force constant. The formula explains the different band centre positions of the different isotopes of ethylene.

Table 2.2 *ν_9 band centres of various isotopes of ethylene* [37]

Molecule	ν_9 band centre (cm^{-1})
$^{12}C_2H_4$	3104
$H_2{}^{12}C{}^{12}CD_2$	3094
$^{12}C_2D_4$	2345
$^{13}C{}^{12}CD_4$	2338
$^{13}C_2D_4$	2326

As shown in Table 2.2, with the substitution of ^{12}C and H atoms with the heavier ^{13}C and D atoms, the band centre is observed at a lower wavenumber. This is because with heavier atoms, the reduced mass of the molecule increases.

2.6 Band classification

The vibrational bands observed in a FTIR spectrum are classified as *A*-type, *B*-type and *C*-type.

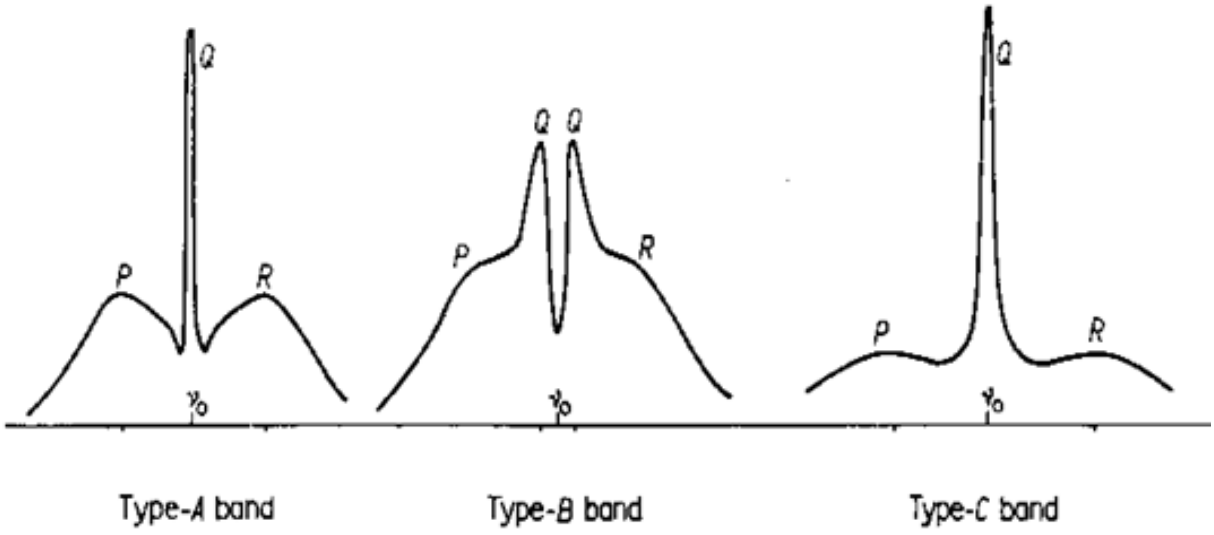

Figure 2.11 *Classification of vibrational bands* [30]

The band type obtained depends on the orientation of transition dipole moment. The *A*-type, *B*-type and *C*-type bands are produced when the transition dipole moment is aligned with the *A* axis, *B* axis and *C* axis respectively. As shown in Figure 2.11, each band has its own characteristic contour. This is because orientation of transition dipole moment affects the possible transitions that can take place. The selection rules for each band type are shown in Table 2.3.

Table 2.3 *Selection rules for A-type, B-type and C-type bands*

Band Type	Selection rules		
A-type:	$\Delta J = 0, \pm 1$	$\Delta K_a = 0, \pm 2$	$\Delta K_c = \pm 1, \pm 3$
B-type:	$\Delta J = 0, \pm 1$	$\Delta K_a = \pm 1, \pm 3$	$\Delta K_c = \pm 1, \pm 3$
C-type:	$\Delta J = 0, \pm 1$	$\Delta K_a = \pm 1, \pm 3$	$\Delta K_c = 0, \pm 2$

Transitions with ΔJ = -1 are known as *P*-branch transitions, transitions with $\Delta J = 0$ are known as *Q*-branch transitions and transitions with ΔJ = +1 are known as *R*-branch transitions. In general, the *P*-branch transitions are at lower wavenumbers, followed by *Q*-branch transitions and the *R*-branch transitions are at higher wavenumbers.

The ν_9 band analysed in the project is a *B*-type band. *B*-type bands have an intensity minimum at the band centre.

A summary of all the vibrational modes of $^{13}C_2D_4$ is given in Table 2.4.

Table 2.4 *Vibrational modes of* $^{13}C_2D_4$ [29, 35]

	Mode	Band Type	Infrared Activity
v_1	CD stretching	-	Infrared inactive
v_2	CC stretching	-	Infrared inactive
v_3	In-plane CD bending	-	Infrared inactive
v_4	CD_2 torsion	-	Infrared inactive
v_5	CD stretching	-	Infrared inactive
v_6	In-plane CD bending	-	Infrared inactive
v_7	Out-of-plane CD bending	*C*-type	Infrared active
v_8	Out-of-plane CD bending	-	Infrared inactive
v_9	CD stretching	*B*-type	Infrared active
v_{10}	In-plane CD bending	*B*-type	Infrared active
v_{11}	CD stretching	*A*-type	Infrared active
v_{12}	In-plane CD bending	*A*-type	Infrared active

2.7 Molecular Symmetry

Molecular symmetry is used to predict if a given band is *A*-type, *B*-type and *C*-type. Each molecule is associated with a given symmetry point group. The group elements are symmetry operations which transform the reference configuration onto itself [27]. Point group elements can be the identity element (*E*), reflection in a given plane (σ_{xy}, σ_{xz}, σ_{yz}), inversion about the origin (*i*) and rotation about an axis by $2\pi k/n$ (C_n *(x),* C_n *(y),* C_n *(z)*). The energy of molecules is invariant under symmetry operations.

Each point group has its own character table. The $^{13}C_2D_4$ molecule belongs to the D_{2h} point group, and the character table is shown in Table 2.5.

Table 2.5 *Character table of D_{2h} point group* [32, 35]

	E	σ_{xy}	σ_{xz}	σ_{yz}	i	$C_2(z)$	$C_2(y)$	$C_2(x)$	Rotation	Vibration
A_g	1	1	1	1	1	1	1	1		ν_1, ν_2, ν_3
A_u	1	-1	-1	-1	-1	1	1	1		ν_4
B_{1g}	1	1	-1	-1	1	1	-1	-1	R_y	ν_5, ν_6
B_{1u}	1	-1	1	1	-1	1	-1	-1		ν_7
B_{2g}	1	-1	1	-1	1	-1	1	-1	R_x	ν_8
B_{2u}	1	1	-1	1	-1	-1	1	-1		ν_9, ν_{10}
B_{3g}	1	-1	-1	1	1	-1	-1	1	R_z	
B_{3u}	1	1	1	-1	-1	-1	-1	1		ν_{11}, ν_{12}

As shown in Table 2.5, there are 8 elements in the D_{2h} group, namely E, σ_{xy}, σ_{xz}, σ_{yz}, $C_2(z)$, $C_2(y)$ and $C_2(x)$. A_g, A_u, B_{1g}, B_{1u}, B_{2g}, B_{2u}, B_{3g}, B_{3u} are the irreducible representations of the D_{2h} point group. The subscripts g and u describes if the electronic wavefunction is symmetric or anti-symmetric with respect to inversion, i. The irreducible representation corresponding to each rotation and vibration mode can be deduced by referring to the last two columns of the table. The character table contains a list of characters, and the characters are calculated from the trace of matrices corresponding to the symmetry transformation.

Different isotopes of ethylene belong to different point groups. For example, the $^{13}C^{12}CH_4$ molecule has C_{2v} symmetry [38] while the $^{12}C_2HD_3$ molecule has C_s symmetry [22]. Thus, the symmetry operations associated with each isotopologue is different. Besides, the point group associated with the molecule will also affect the symmetry of a given vibrational band.

The ν_9 band analysed in this work is a result of transition from the ground vibrational state of A_g symmetry to the excited state of B_{2u} symmetry. According to O. N. Ulenikov *et al.*

[35], the transition from A_g band to B_{2u} band will result in a *B*-type band. The observed spectrum is indeed a *B*-type band, and the observation verifies the prediction based on symmetry.

2.8 Inertial Defect

According to the perpendicular axis theorem [39],

$$I_C = I_A + I_B \tag{2.48}$$

for planar molecules. However, due to out-of-plane molecular vibrations, the ethylene molecule is not planar anymore and the perpendicular axis theorem does not hold for the molecule.

The inertial defect, Δ, has been introduced to quantify non-planarity, and is calculated from the following equation[27]

$$\Delta = I_C - I_A - I_B \tag{2.49}$$

The inertial defect value for planar molecules is zero or close to zero, while the inertial defect value for non-planar molecules is negative. From the calculated inertial defect, approximations of the force constants of vibration can be made [39]. Furthermore, the inertial defect will assist in the accurate determination of molecular structure, in particular, the planarity of the molecule [39].

2.9 Ground State Combination Differences (GSCDs)

To obtain accurate ground state constants, the energy differences between two different rotational states in the ground vibrational state must be calculated. The calculation is carried out using the Ground State Combination Differences (GSCDs) method. The combination difference is calculated by considering the difference in transition wavenumbers for two observed transitions having a common excited state [36]. The method of GSCDs is illustrated in Figure 2.12. In the figure, the observed transitions are denoted by P (J+1), Q (J) and R (J-1). ΔE_{PR}, ΔE_{PQ} and ΔE_{QR} are calculated using the following equations

$$\Delta E_{PR} = \nu\,[R\,(J\text{-}1)] - \nu\,[P\,(J\text{+}1)] \tag{2.50}$$

$$\Delta E_{PQ} = \nu\,[Q\,(J)] - \nu\,[P\,(J\text{+}1)] \tag{2.51}$$

$$\Delta E_{QR} = \nu[R\,(J\text{-}1)] - \nu\,[Q\,(J)] \tag{2.52}$$

where $\nu\,[P\,(J\text{+}1)]$, $\nu\,[Q\,(J)]$ and $\nu[R\,(J\text{-}1)]$ are the transition wavenumbers for the P transition, Q transition and R transition respectively. As shown in Figure 2.12 and the equations 2.50, 2.51 and 2.52,

$$\Delta E_{PR} = \Delta E_{PQ} + \Delta E_{QR} \tag{2.53}$$

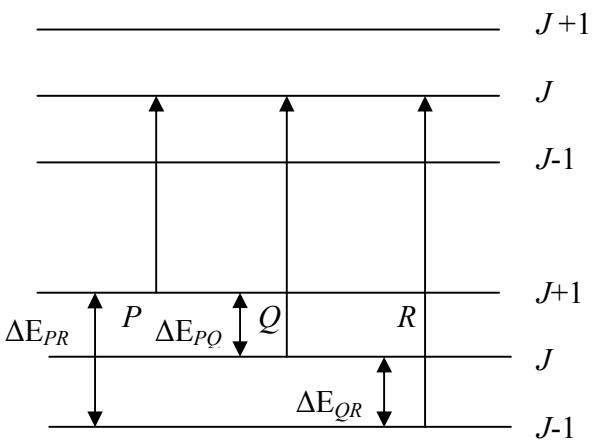

Figure 2.12 *Ground state combination differences denoted by ΔE_{PR}, ΔE_{PQ} and ΔE_{QR}*

CHAPTER 3

FOURIER TRANSFORM INFRARED (FTIR) SPECTROSCOPY

3.1 Michelson Interferometer

Fourier transform infrared (FTIR) spectroscopy was chosen for its ability to produce a high resolution spectrum at a large wavenumber range from 400 cm^{-1} to 4000 cm^{-1} with rapid scanning speed [40]. FTIR spectroscopy is suitable for quantitative and qualitative analysis of solid, liquid and gas samples [1]. The current work involves analyzing transitions between the ground vibrational state and the excited vibrational state, and the transition wavenumbers are in the mid-infrared range, which is within the operating range for FTIR spectroscopy.

The optical system of the FTIR spectrophotometer consists of the Michelson Interferometer. It is connected to a computer, which stores and processes the spectral data collected.

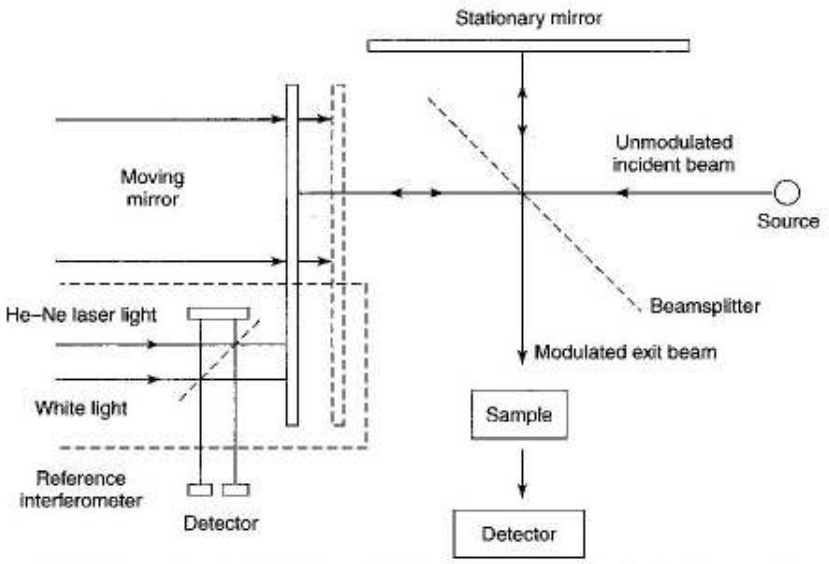

Figure 3.1 *Michelson Interferometer* [1]

The Michelson interferometer set up is shown in Figure 3.1. Infrared (IR) radiation from a source is incident on a beamsplitter. As seen in the figure, a beam of radiation will be reflected onto the stationary mirror, and another beam will be transmitted and be incident on the moving mirror. The moving mirror is perpendicular to the stationary mirror. The beams from both mirrors will be reflected back to the beamsplitter and recombine to give the modulated exit beam. The beam passes through the sample and hits the detector. Due to the different paths taken by both beams, there will be a path difference, x, between the beams. When $x = 0, \lambda, 2\lambda, \ldots$, with λ being the wavelength of the source, the beams are in phase and interfere constructively. When $x = \lambda/2, 3\lambda/2, 5\lambda/2, \ldots$, the beams are out of phase and interfere destructively. Thus, no signal will be detected. When both mirrors are equidistant from the source, there is zero path difference (ZPD) and maximum signal strength is detected.

The signal generated is amplified and converted to digital form. The digital form is a function of intensity against path difference, *f (x)*. For a monochromatic source, *f (x)* behaves like a cosine function

$$f(x) = B(\nu)\cos(2\pi\nu) \tag{3.1}$$

where *B (v)* is the source intensity as a function of frequency, *v*.

However, the source used in the experiment is polychromatic, and *f (x)* is a result of the superposition of cosine functions of different frequencies [1]:

$$f(x) = \int_{-\infty}^{\infty} B(\nu)\cos(2\pi\delta\nu)d\nu \tag{3.2}$$

A typical interferogram of a polychromatic source is shown in Figure 3.2.

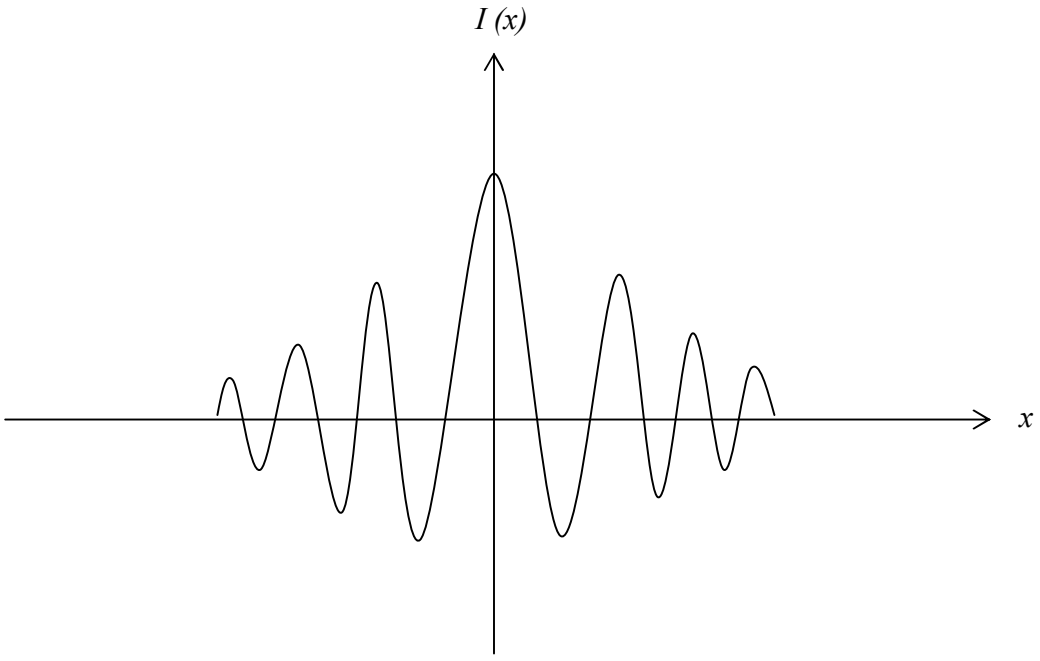

Figure 3.2 *Typical interferogram of a polychromatic source*

A computer receives the digital signal and converts it to a function of intensity against wavenumber, F(ν). The conversion is carried out through Fourier transformation. The mathematical expression describing Fourier transformation [1] is given in equations 3.3 and 3.4.

$$F(v) = \int f(x) e^{-i2\pi vx} dx \tag{3.3}$$

$$f(x) = \int F(v) e^{i2\pi vx} dv \tag{3.4}$$

3.2 Apodization

In Fourier transformation, f(x) and F(ν) are treated as infinite functions. However, f(x) and F(ν) are actually finite functions. Thus, side lobes will be introduced into the spectrum, which is a plot of F(ν). The intensity of interferogram does not fall smoothly to zero. This is illustrated in Figure 3.3.

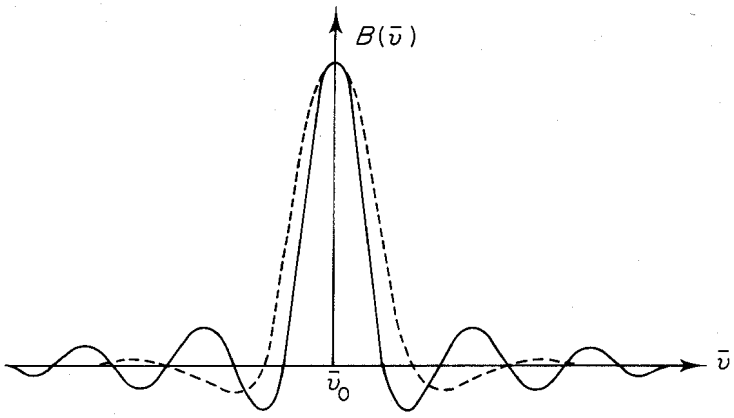

Figure 3.3 *Unapodised signal containing side lobes (solid line) and apodised signal without side lobes (dotted line)* [1]

To remove the side lobes, apodization is carried out. Apodization is a process that multiplies the digital interferogram signal by a function before fourier transformation is carried out. In general, the apodization function used is a cosine function. An example of apodization function is given in equation 3.5, with D being the optical path difference.

$$F(D) = \frac{1 + \cos(\pi D)}{2} \tag{3.5}$$

However, apodization will result in spectral line broadening. Thus, a compromise needs to be made between removing side lobes and minimizing line broadening.

3.3 Resolution

Resolution refers to the ability of the spectrophotometer to distinguish spectral peaks that are close together [41]. Resolution is quantified by the value of Full-Width at Half-Maximum (FWHM) of a strong, unblended line. If lines are not resolved, the observed peak will be blended and peak position will be shifted. There is a limit to resolution, because of factors like Doppler broadening [30]. Doppler broadening is a dominant factor in gases, because the motion of gas molecules is random and this results in peak shifts to both high and low frequencies. Besides, there is inherent line broadening due to the Heisenberg Uncertainty Principle [30]. According to the Heisenberg Uncertainty Principle, there will be some uncertainty in the ro-vibrational energy values and this results in peak broadening.

3.4 Digitisation

Digitisation refers to the process of converting the interferogram, which is an analogue signal, to a digital form so that Fourier Transformation of the interferogram can be carried out [42]. Ideally, an infinite number of data points are needed so that a greater correspondence to the true interferogram shape can be achieved. However, it is impossible to have an infinite number of data points. For a given resolution and spectral range, the optimum number of points required, *N*, is given in equation 3.6 [42].

$$N = \frac{2(\tilde{\nu}_{max} - \tilde{\nu}_{min})}{\Delta\tilde{\nu}} \tag{3.6}$$

$\tilde{\nu}_{max}$ and $\tilde{\nu}_{min}$ refer to the maximum and minimum wavenumber of the spectrum respectively while $\Delta\tilde{\nu}$ refers to the spectral resolution.

3.5 Advantages of FTIR spectroscopy

Before the innovation of FTIR spectrometers, dispersive spectrometers were used. However, dispersive spectrometers have a slow scanning speed [1]. Thus, dispersive spectrometers cannot be used for samples that require a quick measurement.

In contrast, FTIR spectrometers have a quick scanning speed and a high signal-to-noise ratio (SNR). The first advantage associated with the FTIR spectrometer is the Fellgett advantage [1]. The spectrum produced has a high SNR, because a large number of resolution elements are monitored at the same time. Another advantage is the Jacquinot advantage [1]. The spectrum produced has high SNR, because of higher throughput. Throughput is defined as the amount of

light that passes through the circular aperture of the interferometer. Higher throughput is made possible due to the large size of circular aperture. The third advantage is the fast acquisition of spectral data, and with the FTIR spectrometer, it is possible to scan samples that require a quick measurement.

CHAPTER 4

EXPERIMENTAL DETAILS

4.1 Instrumental Setup

The spectrophometer used is the Bruker IFS 125 HR Michelson Fourier Transform Infrared (FTIR) Spectrophotometer, developed by Bruker Corporation, USA. The spectrophotometer used has an unapodised resolution of 0.0063 cm^{-1}, and is usually used for spectroscopy in the mid-infrared region to obtain vibrational spectra. The basic spectrometer configuration includes the Bruker Spectrophotometer connected to the gas handling system and to the computer via the OPUS software. The OPUS software, developed by Bruker Corporation, is used in the instrument control and data acquisition processes. The spectrophotometer has high energy throughput, making it highly sensitive. A photo of the Bruker FTIR spectrophotometer used is shown in Figure 4.1.

Figure 4.1 *Bruker IFS 125 HR Michelson FTIR Spectrophotometer*

The chapter will discuss the components of the spectrophotometer in detail, which includes the source, input system, optical system, control system and analytical software used.

4.2 Source

The source used depends on the choice of spectral range. For the mid-IR range, the Globar or Nerst source is used. For the far IR range, the mercury lamp is used. For the near IR range, the tungsten-halogen lamp is used [1]. In the case of the Bruker IFS 125 HR Michelson FTIR Spectrophotometer, the globar infrared source is used.

4.3 Input system

The input system consists of the following components:

i) sample compartment to accomodate sampling accessories like gas cells

ii) vacuum pump to reduce impurities present in air

iii) absorption cell and

iv) liquid nitrogen cold trap for the condensation of gas vapour from the backstream of the pump

A schematic of the input system is shown in Figure 4.2.

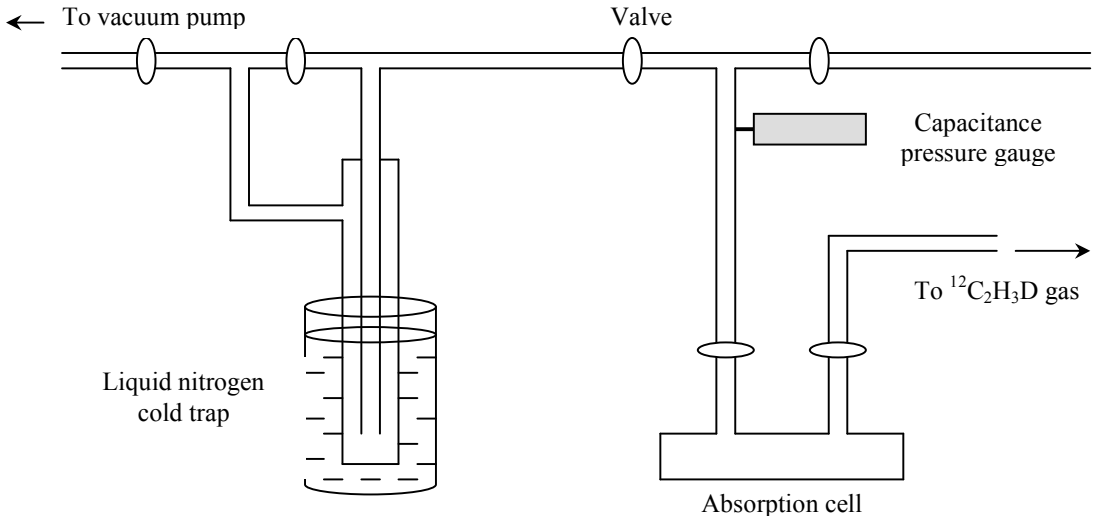

Figure 4.2 *Schematic of input system*

A close up photo of the multi-pass gas cell which contains the gas sample is shown in Figure 4.3.

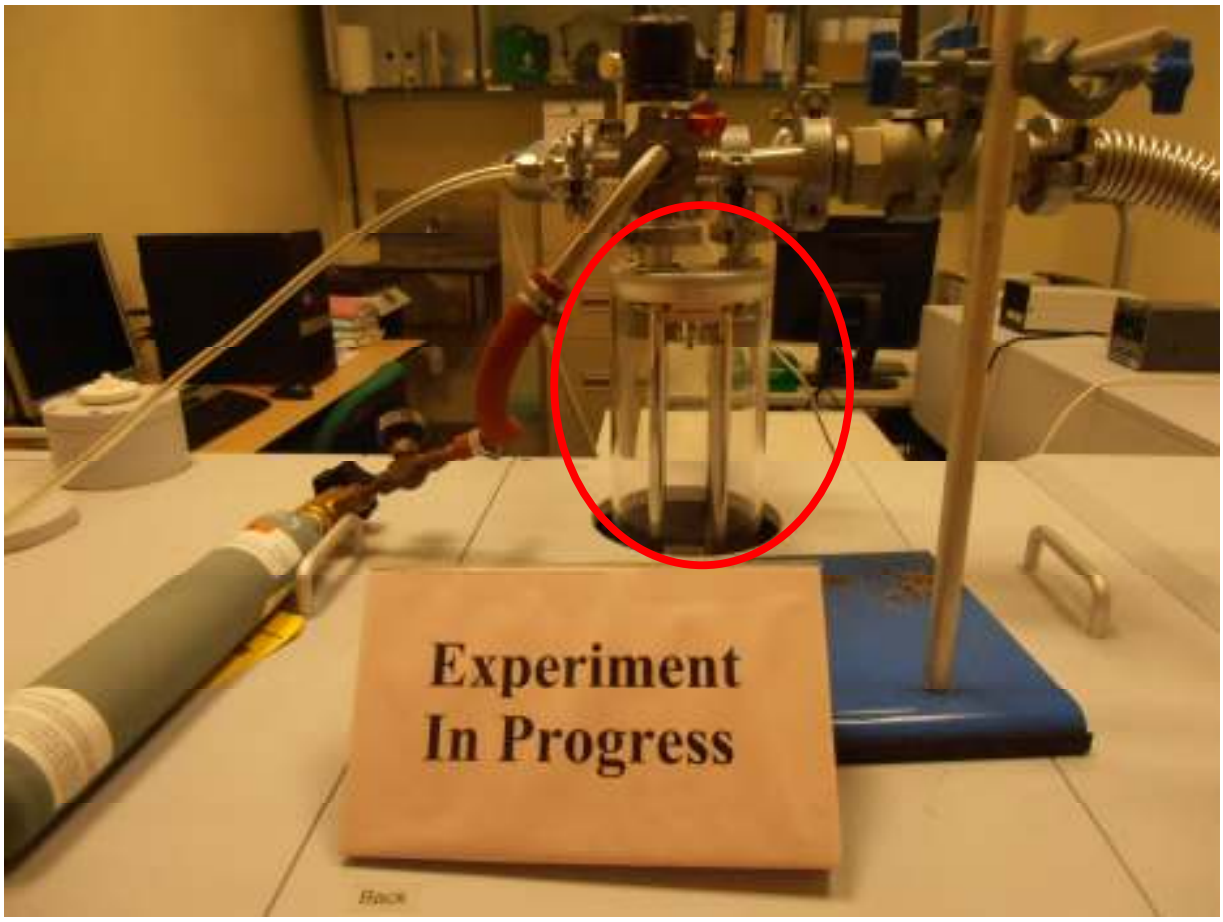

Figure 4.3 *Multi-pass absorption cell (circled in red) containing the gas sample*

4.4 Optical system

The optical system of the Bruker FTIR spectrophotometer used consists of a KBr beam splitter, a high-sensitivity liquid nitrogen cooled Hg-Cd-Te detector, a multi-pass cell (shown in Figure 4.3) and a filter system. KBr is used as a beam splitter because KBr is transparent to IR radiation. The multi-pass cell increases the total optical path length, resulting in the detector

becoming more sensitive to transmitted radiation. The filter system is needed to ensure that the radiation incident on the sample is restricted to the mid-IR range.

4.5 Analytical software

For the Bruker FTIR spectrophotometer, the Optics User Software (OPUS) software is used to set up measurement parameters. For example, detector settings are adjusted with the software. Besides, the software is used to process data collected. For example, Fourier transform is carried out by the software. The recorded spectrum is stored, plotted and viewed using the OPUS software. The spectral data from OPUS can be exported to other software programs for further analysis.

4.6 Spectrum collection and measurements

The experiment was carried out at the National Institute of Education, Nanyang Technological University, Singapore. The spectral measurements were recorded at an ambient temperature of 296 K using a globar infrared source, KBr beam splitter and a high-sensitivity liquid nitrogen cooled Hg-Cd-Te detector. Vapour pressure in the gas cell was monitored with a capacitance pressure gauge and adjusted to 1.41 mbar. An absorption cell with a 20-cm base path was used. A total absorption path length of 80.0 cm was achieved by adjusting for 4 passes in the cell. In general, spectrum collection consisted of the following steps:

1. First, the gas sample was introduced into the gas cell. Subsequently, the sample spectrum was recorded.

2. Next, the gas cell was evacuated to remove the gas that was introduced previously and reduce the amount of impurities like water and carbon dioxide in the cell.

3. A background spectrum of the evacuated cell was collected.

4. The transmittance spectrum was obtained. The transmittance spectrum was obtained using equation 4.1.

$$Transmittance\ Spectrum = \frac{Sample\ Spectrum}{Background\ Spectrum} \tag{4.1}$$

5. The transmittance spectrum was stored in the OPUS software and the spectrum was peak-picked using the software.

6. Calibration of the transmittance spectrum was carried out.

In this work, $^{13}C_2D_4$ gas samples of 98 % purity were purchased from Cambridge Isotope Laboratories, USA. The $^{13}C_2D_4$ gas was introduced into the gas cell. Immediately after the sample was introduced into the gas cell, the ν_9 band of $^{13}C_2D_4$ was recorded by the Bruker IFS 125 HR Michelson FTIR spectrophotometer at an unapodised resolution of 0.0063 cm^{-1}. The total scanning time was about 18 hours with 1000 scans. Subsequently, a background spectrum of the evacuated cell consisting of 100 scans was collected. The transmittance spectrum in the wavenumber range from 2230 cm^{-1} to 2460 cm^{-1} was obtained.

4.7 Calibration

Calibration was carried out to reduce the effects of systematic errors caused by instrumental shift. Calibration of the absorption lines of ν_9 of $^{13}C_2D_4$ was done using 38 strong and unblended CO_2 lines in the range of 2298 cm^{-1} to 2377 cm^{-1}. A least-squares fitting program written by A. G. Maki [43-45] was used in the calibration of the observed frequencies against the standard frequencies. The calibration process involved the use of a program to carry out least-squares fitting. The CO_2 lines were used because they are in the same frequency as the ν_9 band of $^{13}C_2D_4$, which lies in the range of 2230 cm^{-1} to 2460 cm^{-1}. The measured CO_2 transition wavenumbers were compared with selected CO_2 standard lines, taken from reference [46]. The correlation coefficient of r = 1.0000 shows that there is a linear relationship between standard frequency and observed frequency. Figure 4.4 shows two of the selected CO_2 lines used for calibration.

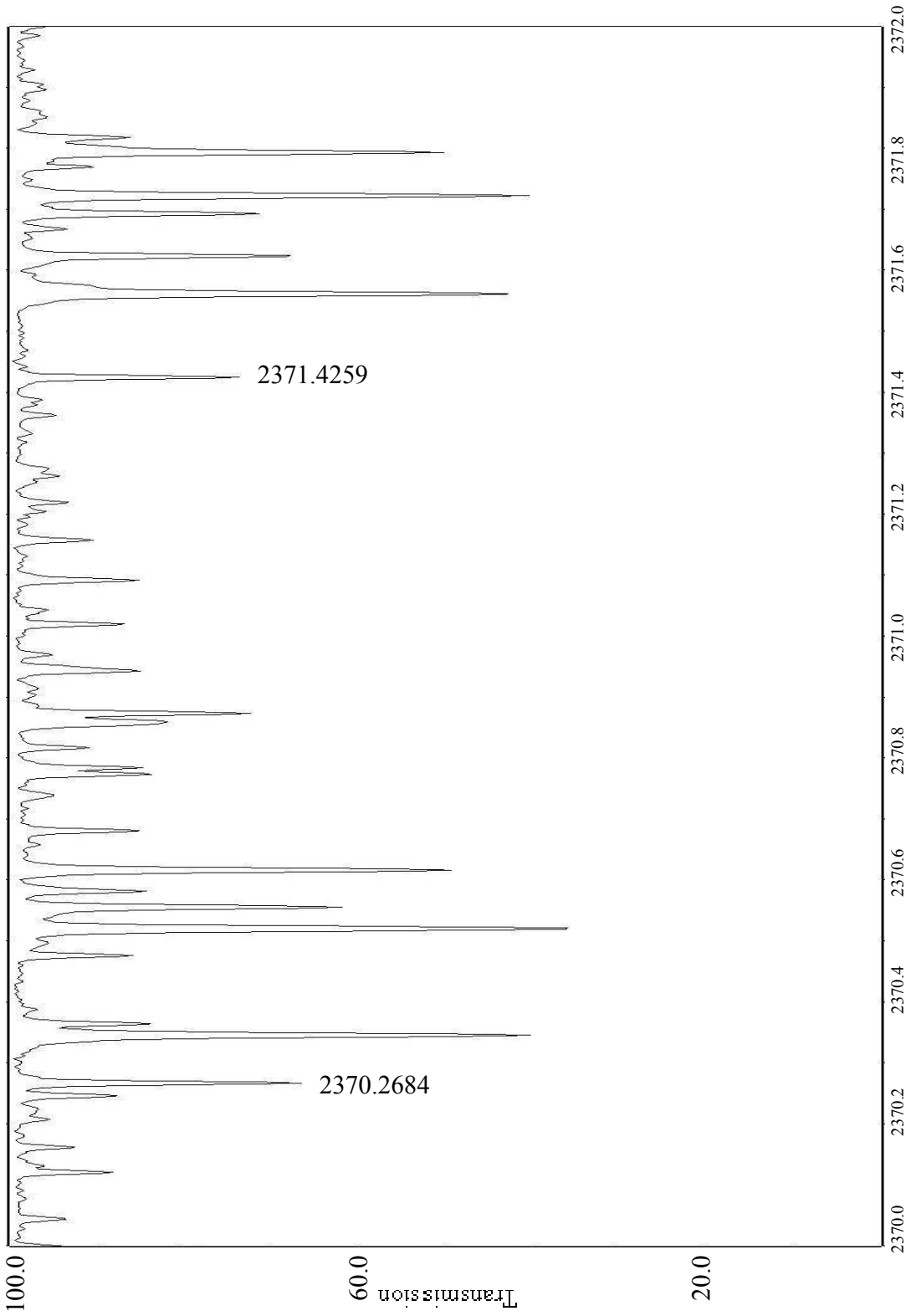

Figure 4.4 *Two of the selected CO_2 spectral lines from the recorded $^{13}C_2D_4$ ν_9 band used for calibration*

A graph of standard frequency, S, against observed frequency, O, is shown in Figure 4.5.

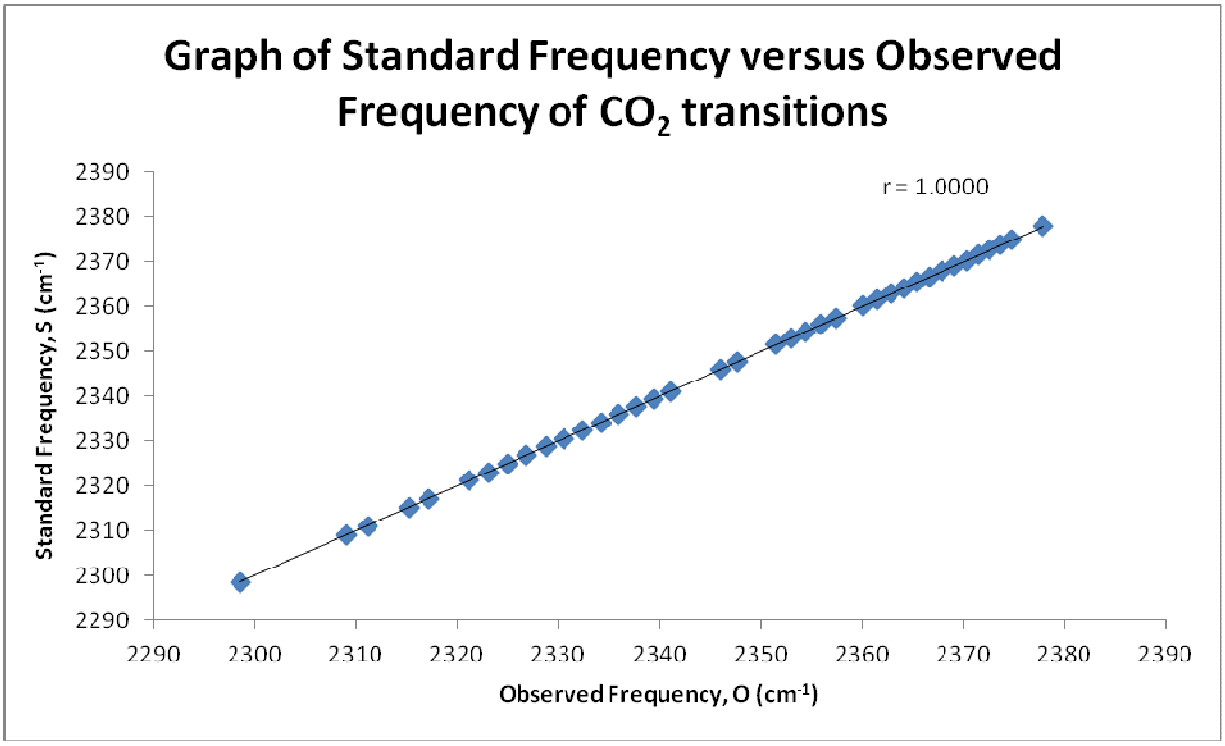

Figure 4.5 *Graph of Standard Frequency against Observed Frequency*

A correction factor of 1.0000001032 was required to bring the observed frequency into agreement with the calibrated frequency. A total of 38 standard frequency values were fitted, and the standard error of the fitted lines was found to be 0.0002 cm^{-1}. Accounting for systematic errors, the absolute uncertainty is approximated to be ± 0.0005 cm^{-1}. The calibration frequencies, observed values and corrections are given in Table 4.1.

Table 4.1 *Infrared lines of CO_2 used for calibration of v_9 band of $^{13}C_2D_4$*

Line No.	Standard Frequency, S	Observed Frequency, O	S-O (cm^{-1})	Fit-O (cm^{-1})	S-Fit (cm^{-1})
1	2298.540870	2298.540700	0.000170	0.000237	-0.000067
2	2309.027910	2309.027500	0.000410	0.000238	0.000171
3	2311.105840	2311.105100	0.000740	0.000239	0.000500
4	2315.189510	2315.189400	0.000110	0.000239	-0.000129
5	2317.195190	2317.195200	-0.000010	0.000239	-0.000249
6	2321.134110	2321.133900	0.000210	0.000240	-0.000030
7	2323.067300	2323.067300	0.000000	0.000240	-0.000240
8	2324.976260	2324.976000	0.000260	0.000240	0.000019
9	2326.860970	2326.861000	-0.000030	0.000240	-0.000270
10	2328.721410	2328.721200	0.000210	0.000240	-0.000030
11	2330.557540	2330.557000	0.000540	0.000241	0.000298
12	2332.369340	2332.368700	0.000640	0.000241	0.000398
13	2334.156780	2334.156600	0.000180	0.000241	-0.000061
14	2335.919840	2335.919600	0.000240	0.000241	-0.000001
15	2337.658490	2337.658600	-0.000110	0.000241	-0.000351
16	2339.372690	2339.372500	0.000190	0.000241	-0.000051
17	2341.062440	2341.062200	0.000240	0.000242	-0.000002
18	2345.984610	2345.984300	0.000310	0.000242	0.000067
19	2347.576230	2347.575400	0.000830	0.000242	0.000587
20	2351.447630	2351.447400	0.000230	0.000243	-0.000013
21	2352.953060	2352.952800	0.000260	0.000243	0.000016
22	2354.433800	2354.433500	0.000300	0.000243	0.000056
23	2355.889830	2355.889700	0.000130	0.000243	-0.000113
24	2357.321130	2357.320300	0.000830	0.000243	0.000586
25	2360.109430	2360.109200	0.000230	0.000244	-0.000014
26	2361.466380	2361.466100	0.000280	0.000244	0.000035
27	2362.798500	2362.798400	0.000100	0.000244	-0.000144
28	2364.105760	2364.105600	0.000160	0.000244	-0.000084
29	2365.388130	2365.388000	0.000130	0.000244	-0.000114
30	2366.645600	2366.645500	0.000100	0.000244	-0.000144
31	2367.878150	2367.878000	0.000150	0.000244	-0.000094
32	2369.085740	2369.085500	0.000240	0.000244	-0.000004
33	2370.268350	2370.267900	0.000450	0.000245	0.000204
34	2371.425960	2371.425800	0.000160	0.000245	-0.000085
35	2372.558550	2372.558600	-0.000050	0.000245	-0.000295
36	2373.666090	2373.665800	0.000290	0.000245	0.000044

Line No.	Standard Frequency, S	Observed Frequency, O	S-O (cm^{-1})	Fit-O (cm^{-1})	S-Fit (cm^{-1})
37	2374.748560	2374.748400	0.000160	0.000245	-0.000085
38	2377.845330	2377.845400	-0.000070	0.000245	-0.000315

Note:
1. Root-mean-square (rms) error of the fitting is 0.0002268 cm^{-1}.
2. Least-squares fitting used is 38 points.

4.8 Signal-to-Noise (SNR) ratio

During the process of spectral line assignment, it is important to distinguish spectral peaks from noise. Noise refers to random signals generated by the source or detector. If noise is inaccurately assigned to be a spectral peak, the set of ro-vibrational constants generated from fitting will also predict noise. The signal-to-noise ratio is lower for spectral peaks corresponding to higher J' values, which are weaker in intensity. The SNR for a real spectral peak should be at least 3.

To maximize the signal-to-noise ratio, more number of scans is used to collect the spectrum. This is because the SNR is proportional to the square root of the number of scans, n [1]:

$$SNR \alpha \sqrt{n} \tag{4.2}$$

CHAPTER 5

SPECTRAL ANALYSIS

5.1 Assignment and frequency analysis

The $^{13}C_2D_4$ molecule is a planar asymmetric molecule. As mentioned in section 2.3.4, for the $^{13}C_2D_4$ molecule, $I_A < I_B < I_C$. The directions of the *A, B* and C axes corresponding to I_A, I_B and I_C respectively are shown in Figure 5.1.

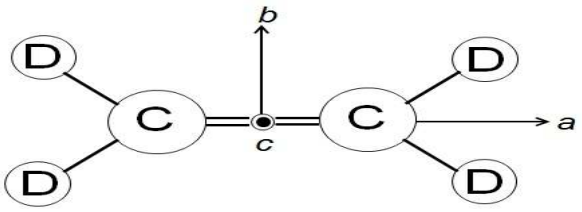

Figure 5.1 *$^{13}C_2D_4$ molecule*

The *A* axis is along the C=C bond, the *B* axis is in the molecular plane while the *C* axis is perpendicular to the molecular plane.

The ν_9 mode is one of the 12 vibrational modes of ethylene, and it corresponds to C-D stretching[25, 29]. The ν_9 mode is illustrated in Figure 5.2. The ν_9 mode is infrared active and has B_{2u} symmetry [29].

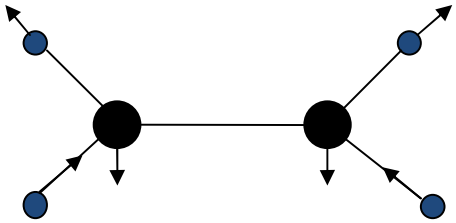

Figure 5.2 *ν_9 vibrational mode*

The spectrum of the entire ν_9 vibrational band is shown in Figure 5.3. The spectrum was recorded in the wavenumber range from 2240 cm^{-1} to 2420 cm^{-1}. The band centre is at 2324.36 cm^{-1}. The *P*-branch lines are to the left of the band centre, at lower wavenumbers while the *R*-branch lines are to the right of the band centre, at higher wavenumbers.

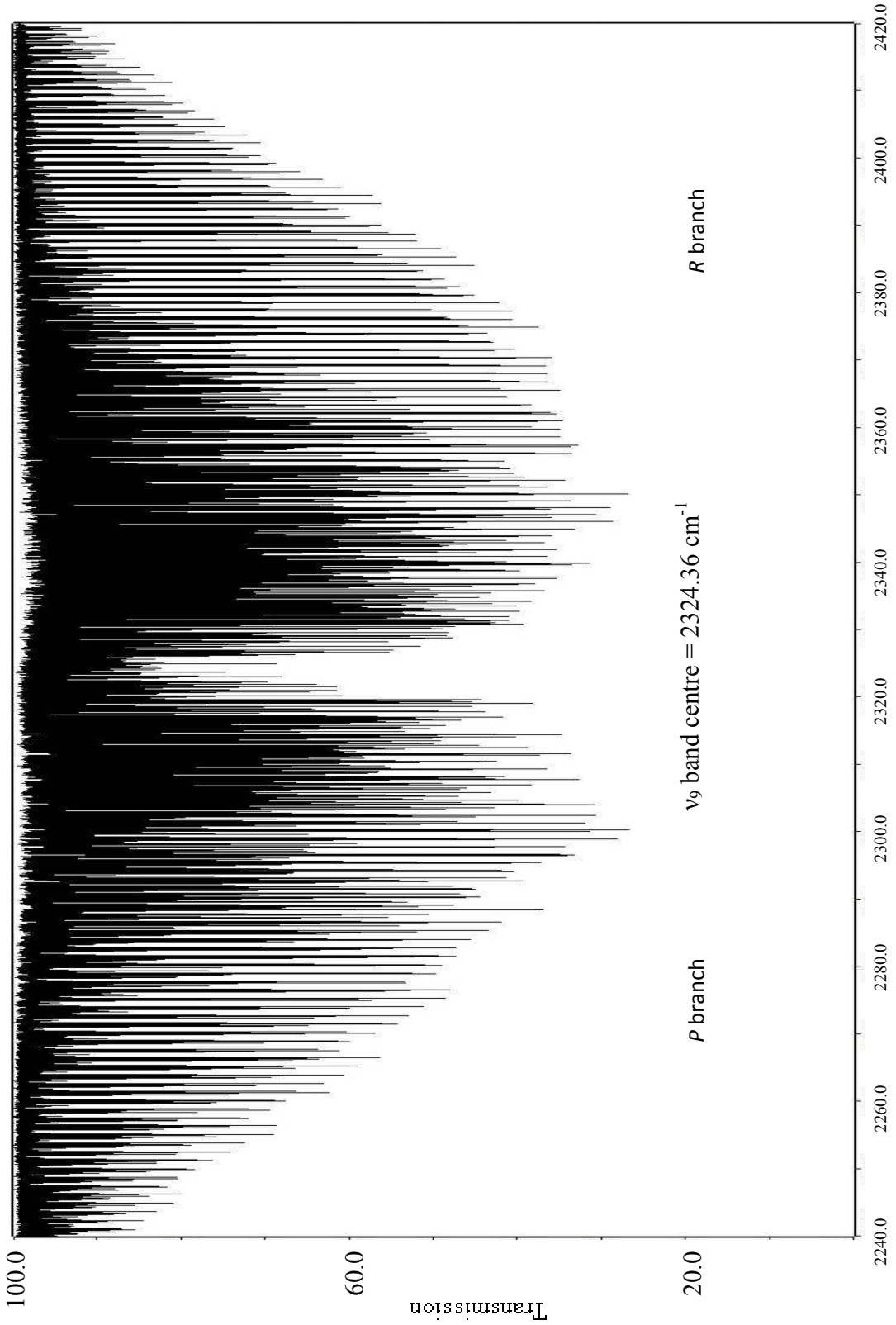

Figure 5.3 The ν_9 vibrational band of $^{13}C_2D_4$

A qualitative approach in identifying the type of band is by observing the band contour. As shown in Figure 5.3, the vibrational band has a minimum at the band centre, which is a distinctive feature of *B*-type bands. Thus, the strongest transitions are determined by the following selection rules

$$\Delta J = 0, \pm 1; \qquad \Delta K_a = \pm 1; \qquad \Delta K_c = \pm 1 \tag{5.1}$$

5.2 General Appearance of Spectrum

The peak intensities are dependent on the populations of rotational energy levels in the ground vibrational state. The population of each energy level is affected by two factors, firstly, the Boltzmann distribution and secondly, the degeneracy [30]. According to the Boltzmann distribution, the ratio of population on excited state, N_J, to the population on the ground state, N_0, is related by an exponential term, as shown in the following equation

$$\frac{N_J}{N_0} = e^{-\alpha J(J+1)} \tag{5.2}$$

α is a parameter affected by temperature and moment of inertia.

Different states having the same energy are said to be degenerate. A given rotational energy state having rotational quantum number J is $2J+1$ degenerate. By considering the Boltzmann distribution and the degeneracy, N_J and N_0 are related by the following equation

$$\frac{N_J}{N_0} = (2J+1)e^{-\alpha J(J+1)} \tag{5.3}$$

For energy levels with low J, the linear term $2J+1$ dominates and peak intensity increases with increasing J. However, as J gets larger, the exponential term will dominate. Thus, intensity increases with J, reaches a peak and then decreases.

Unlike *A*-type and *C*-type bands where there are distinct *Q* branch clusters near the band centre, for the *B*-type band, there are no distinct *Q* branch clusters which can be observed near the band centre.

5.3 Assignment of Quantum Numbers

Spectral line assignment refers to the process of attributing the final energy state and initial energy state associated with each spectral peak. The initial energy state is labeled by the quantum numbers J'', K_a'' and K_c'' while the final energy state is labeled by J', K_a' and K_c'.

The Loomis-Wood software, written by D. McNaughton *et al.*[47], was used to analyse the observed spectral peaks. The ν_9 spectrum collected in this work was peak-picked using OPUS software and presented in the Loomis-Wood format using MacLoomis, which groups regularly spaced lines, such as those differing in J but sharing constant K_a, into approximately vertical series of constant K_a. Presenting the spectra in this way allowed series up to K_a' =14 to be assigned quantum numbers, with a maximum J' value of 31.

A program called Asymb9 written in Fortran language by A. G. Maki [44, 45] was used to calculate energy values for the different energy states based on a Watson's A-reduced Hamiltonian [48] in I^r representation. The input file involved contains estimates of the ground state and upper state constants. The ground state constants were taken from analysis on the ν_{12}

band of $^{13}C_2D_4$ reported by T.L. Tan *et al.*[24]. The input file of constants was updated each time the ground state or upper state constants were improved. From calculated energy values for different energy levels, the program is able to generate a set of calculated transition wavenumbers with the corresponding J, K_a and K_c quantum numbers. The calculated transition wavenumbers predict the positions of spectral peaks.

The calculations served as a reference and assisted in matching the observed peak positions with the calculated peak positions. After matching was done, trial and error assignment of the quantum numbers associated with each peak was carried out. The assignment was done on a peaklist file containing the observed peak positions of all the spectral peaks. After spectral peaks were assigned, least-squares fitting was carried out to get improved upper state constants. In the process, the ground state constants were fixed to fit the upper state (ν_9=1) constants. A schematic illustrating the spectral line assignment process is shown in Figure 5.4. Details of spectral line assignments for the *P*-branch, *Q*-branch and *R*-branch are shown in Figures 5.5, 5.6 and 5.7 respectively.

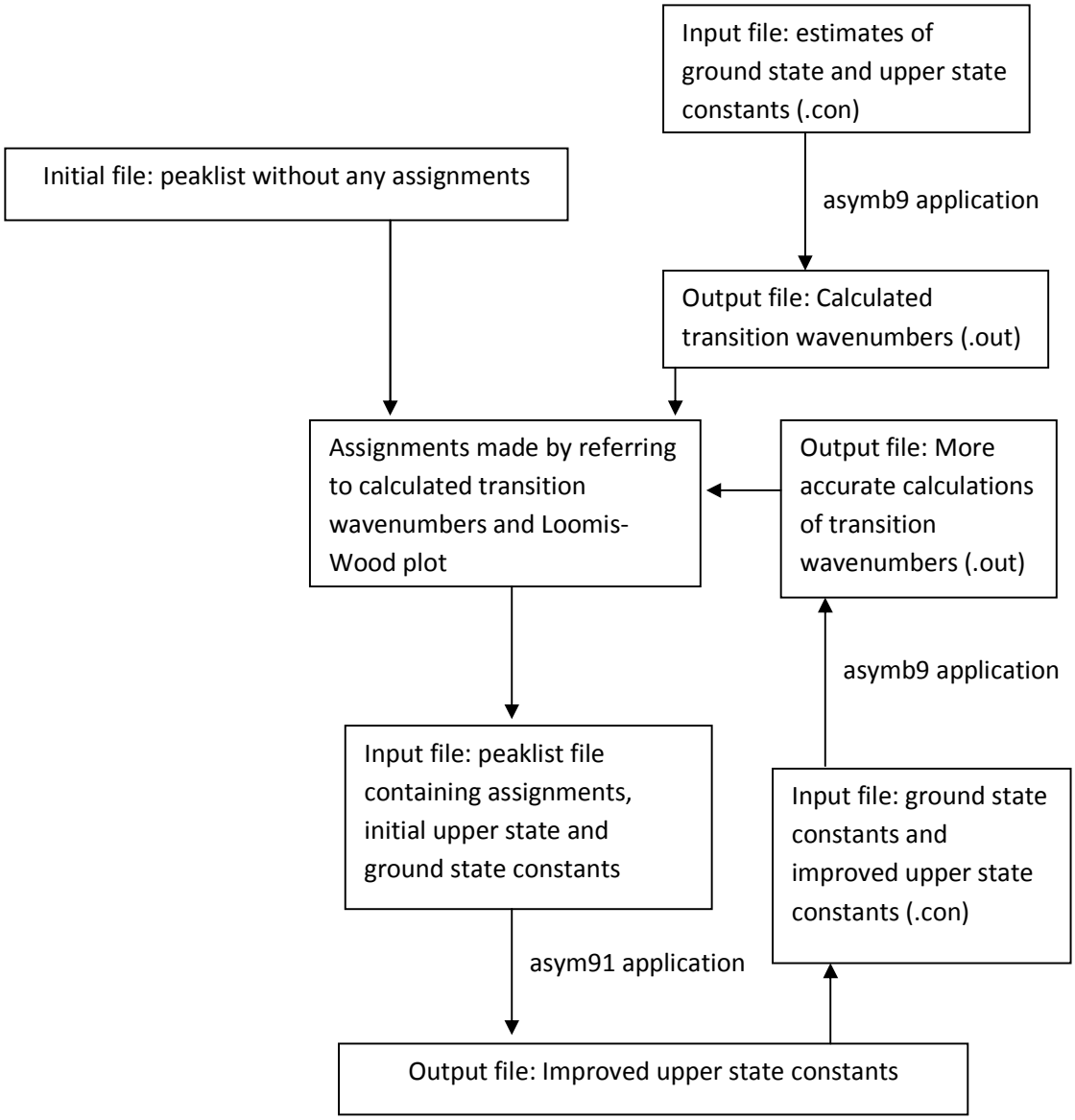

Figure 5.4 *Spectral line assignment process*

Note: Both the asym91 and asymb9 applications were written by A. G. Maki [44,45] and this work involves the use of both applications to derive improved upper state constants

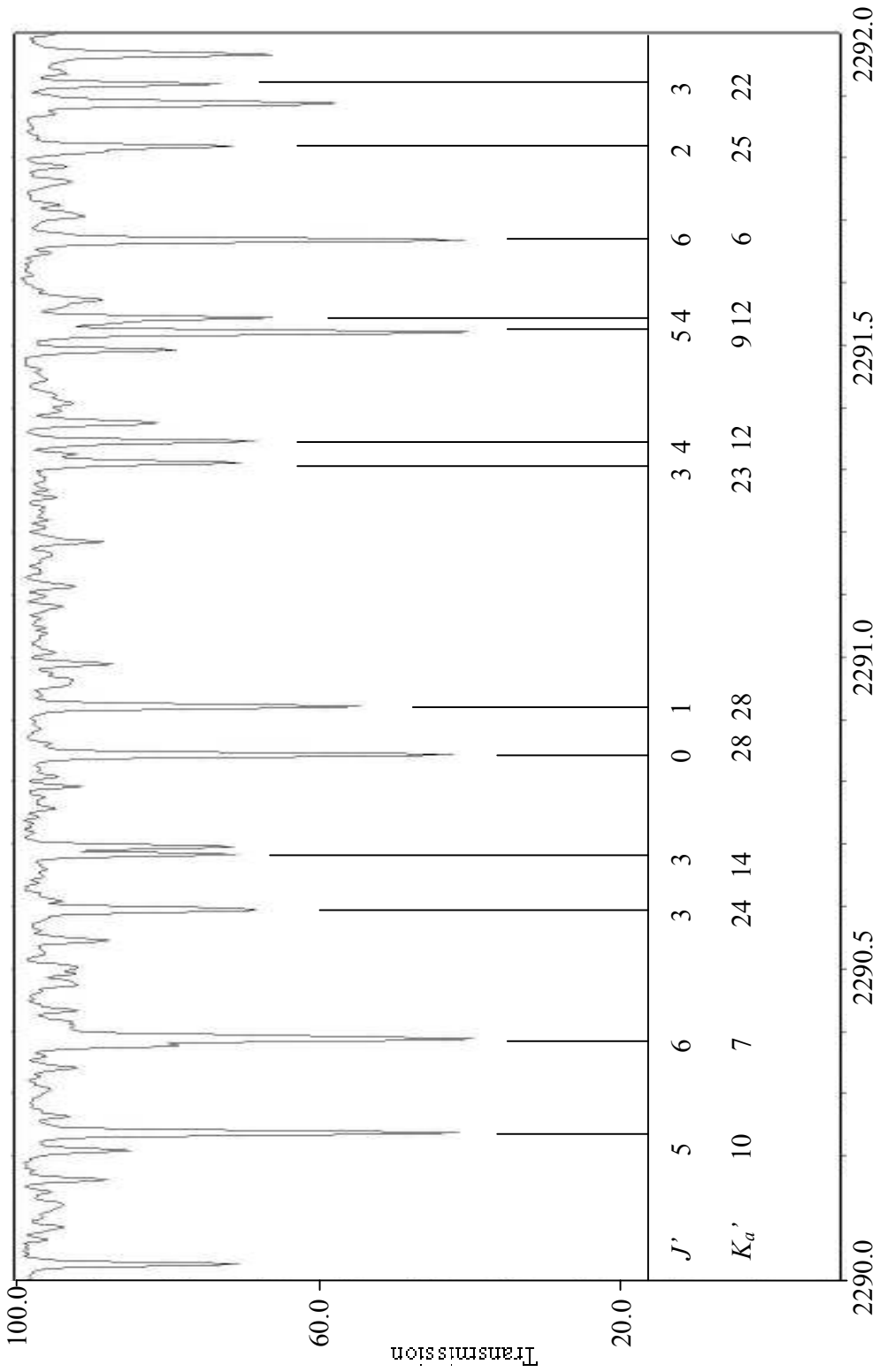

Figure 5.5 *Detailed spectrum of the ν_9 band of $^{13}C_2D_4$ showing the P-branch lines*

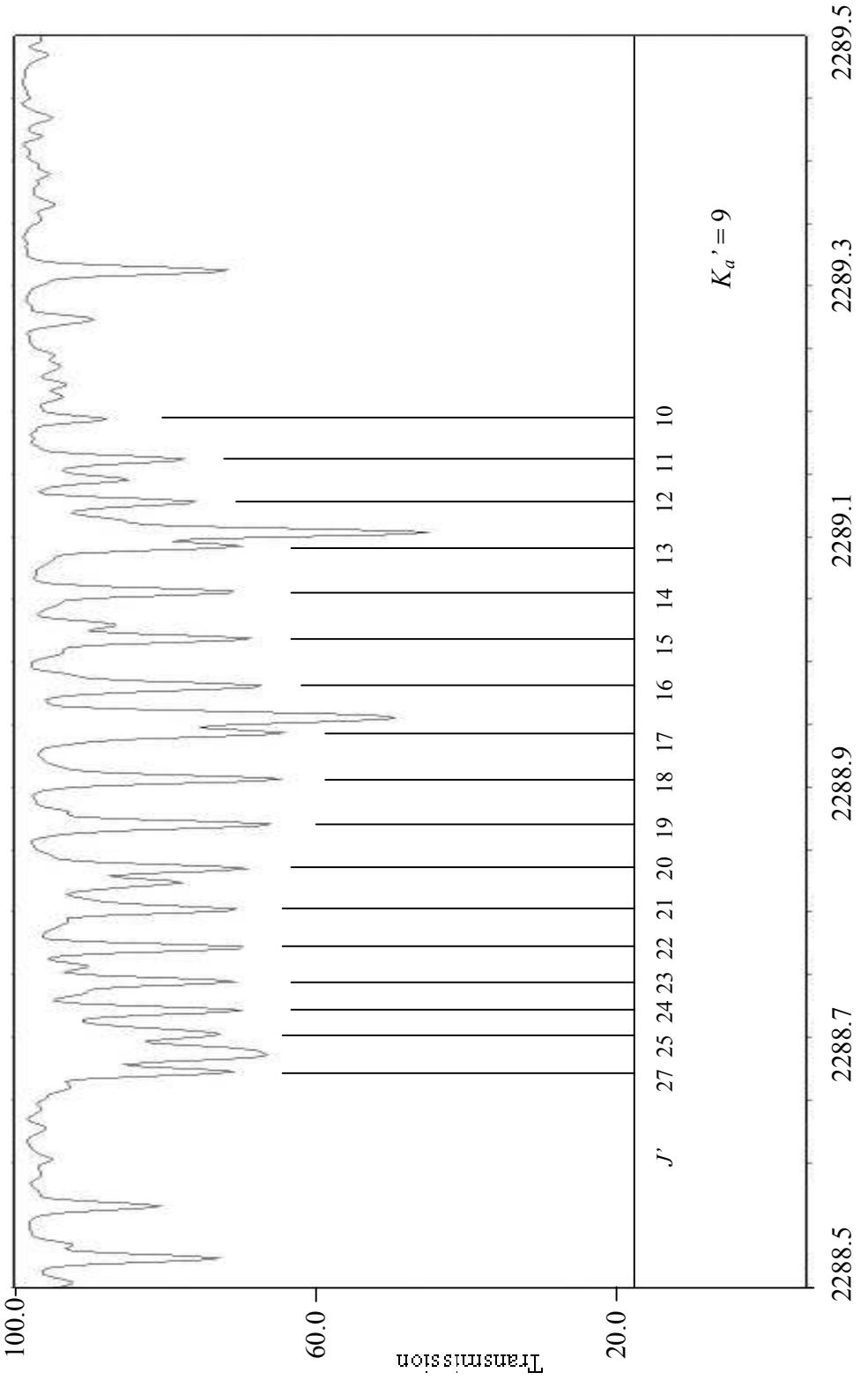

Figure 5.6 *Detailed spectrum of the ν_9 band of $^{13}C_2D_4$ showing the Q-branch series*

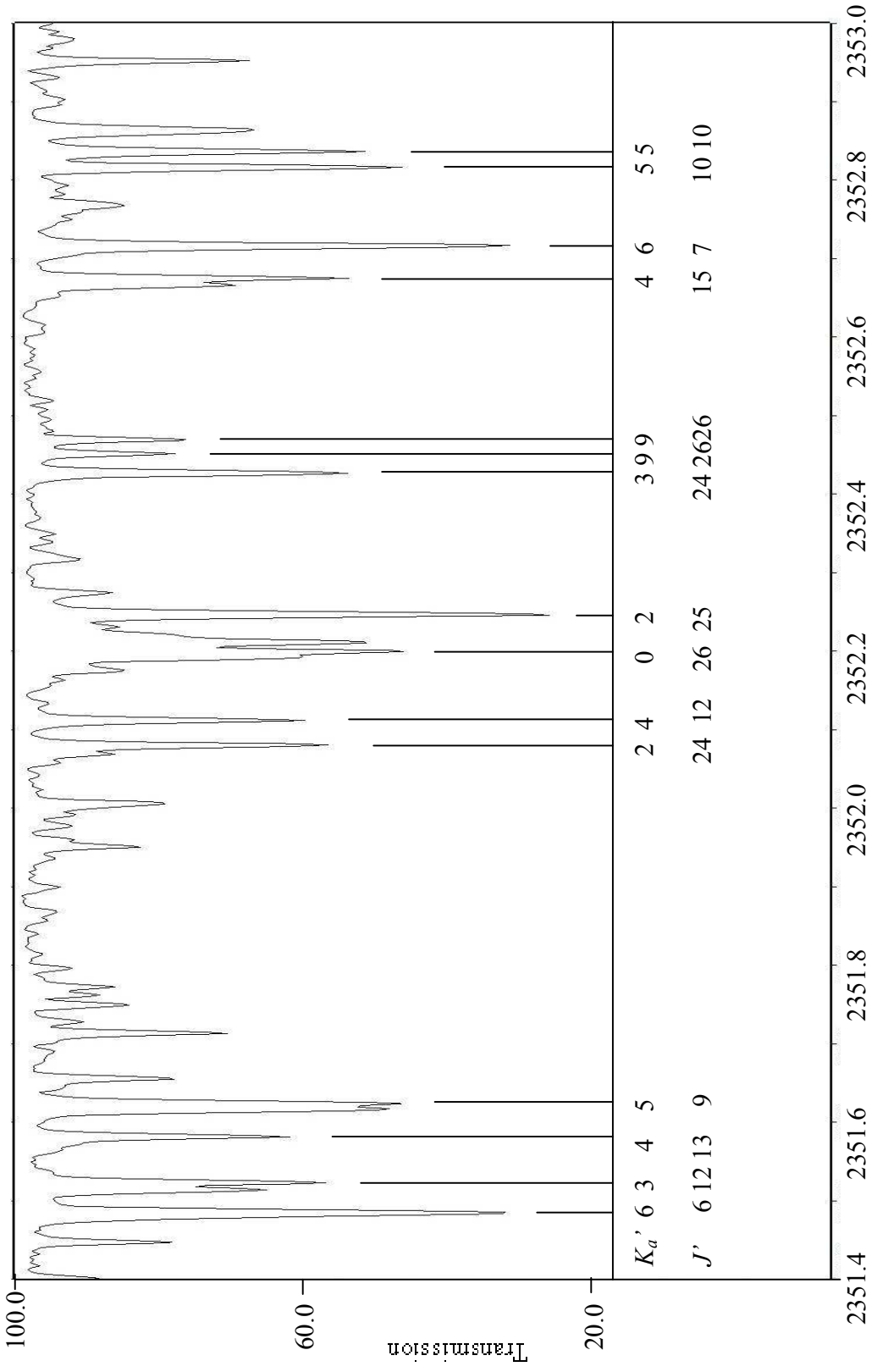

Figure 5.7 *Detailed spectrum of the ν_9 band of $^{13}C_2D_4$ showing the R-branch lines*

The ground state constants were fixed and the peaks corresponding to low J' and K_a' values were assigned first. Subsequently, a least squares fitting program written by A. G. Maki [44, 45] was used to improve the accuracy of the upper state constants. The improved upper state constants were used to derive a new set of calculated transition wavenumbers.

The observed peak positions were then compared with the new set of calculated transition wavenumbers. The deviation between the observed wavenumbers and calculated wavenumbers was quantified by the root mean square (rms) value. The rms value gives an indication of how accurate the assignments were. A cutoff deviation of 0.00100 cm^{-1} was set, and any assigned peak having a deviation larger than the cutoff was excluded from the fitting analysis.

With the improved set of calculations, the peaks corresponding to higher J' and K_a' values were assigned. Fitting was carried out periodically after additional series were assigned. Each round of spectral line assignment stopped when all the lines with deviation less than the cutoff value had been assigned. The process of deriving improved upper state constants was repeated. With each round of improvement, the input file containing the constants was updated and a new set of transition wavenumbers was calculated using the fitting program. After that, additional spectral lines were assigned. The additional assignments had large deviations previously, but the deviations were within the acceptable range after the upper state constants were improved. With the additional assignments, derivation of more accurate upper state constants was achieved. Fitting stopped when no more lines can be assigned with confidence.

Besides refining the upper state constants, the ground state constants were refined by the method of Ground State Combination Differences (GSCDs), discussed previously in section 2.9. From spectral line assignments, the fitting program calculates the energy differences between

rotational energy levels in the ground vibrational state and from the energy differences, the program predicts the ground state constants.

Peaks associated with high J, K_a and K_c values are usually perturbed. Even though the assignments were correct, the deviation for the peaks exceeded the cutoff deviation of 0.0010 cm^{-1}. Thus, peaks having J' value greater than 30 (for the P branch) and peaks having J' value greater than 32 (for the Q and R branches) were excluded from the fit.

Besides the perturbed peaks, other peaks that were excluded from the fit include the peaks due to impurities like water and carbon dioxide and unresolved peaks that were not fully resolved due to the limited resolution of the spectrophotometer.

5.4 Results and Discussion

The Watson's A-reduced Hamiltonian in I^r representation [28] has the form

$$\hat{H}_{rot} = BP_x^2 + CP_y^2 + AP_z^2 - \Delta_J (P^2)^2 - \Delta_{JK} P^2 P_z^2 - \Delta_K P_z^4 - \frac{1}{2}\left[\delta_J P^2 + \delta_K P_z^2, P_+^2 + P_-^2\right]_+$$

where $\boldsymbol{P}^2 = \boldsymbol{P}_x^2 + \boldsymbol{P}_y^2 + \boldsymbol{P}_z^2$ and $\boldsymbol{P}_-^2 = \boldsymbol{P}_x^2 + \boldsymbol{P}_y^2$. (6.4)

The constants A, B and C are rotational constants associated with rotation about the A-axis, B-axis and C-axis respectively. The A-axis, B-axis and C-axis of the ethylene molecule are shown in Figure 5.8a while the choice of x-axis, y-axis and z-axis is shown in Figure 5.8b.

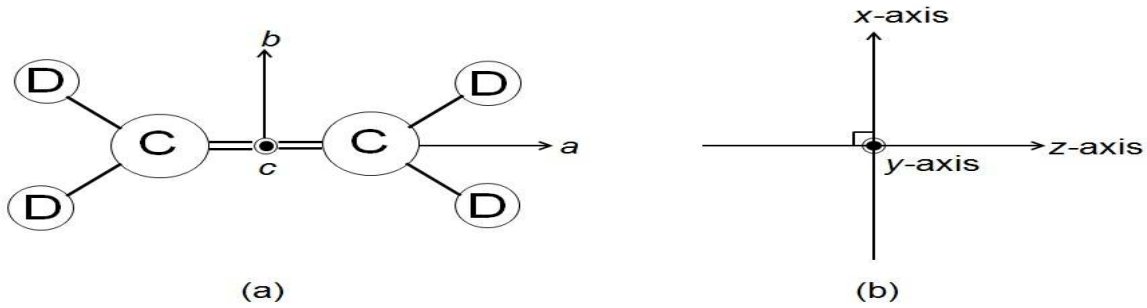

Figure 5.8 (a) *A-axis, B-axis and C-axis of the ethylene molecule* and (b) *Choice of x-axis, y-axis and z-axis in I^r representation*

Δ_J, Δ_{JK}, Δ_K, δ_J and δ_K are quartic constants (fourth degree centrifugal terms). The quartic terms account for the change in energy due to centrifugal distortion of the bond. Due to rotational motion, the atoms experience centrifugal force. For states with higher J values, the bond length increases and the actual rotational energy is reduced.

The derived upper state and ground state constants consisting of 3 rotational and 5 quartic constants are shown in Table 5.1.

Table 5.1 *Ground State and Upper State (ν_9=1) Constants (cm^{-1}) for $^{13}C_2D_4$*

	Ground State (cm^{-1}) (T.L. Tan *et al.*)	**Ground State (cm^{-1}) (this work)**	**Upper state (ν_9=1) (cm^{-1}) (this work)**
A	2.441678 (32)	2.441700 (19) [a]	2.4324237 (11)
B	0.70745636 (77)	0.70745755 (55)	0.70541070 (77)
C	0.54723410 (79)	0.54723316 (50)	0.54577249 (96)
Δ_J x 10^6	0.73704 (29)	0.73648 (28)	0.7272 (29)
Δ_{JK} x 10^5	0.27457 (33)	0.27536 (29)	0.3090 (16)
Δ_K x 10^4	0.2125 (45)	0.20634 (10)	0.20660 (16)
δ_J x 10^6	0.19029 (12)	0.19043 (14)	0.1471 (22)
δ_K x 10^5	0.3735 (14)	0.36950 (91)	0.221 (10)
ν_0	-	-	2324.359306 (27)
No. of IR transitions	985	1677 [b]	1281
RMS deviations (cm^{-1})	0.00036	0.000395	0.000428
Δ_{12} (μ Å^2)	0.07253 (16)	0.0727254 (33)	0.0596918 (28)

[a] The uncertainty in the last digits (twice the estimated standard error) is given in parentheses.
[b] For the ground state the number of infrared transitions is actually the number of combination differences used in the fit.

In this work, 1281 transitions (421 P-branch, 408 Q-branch and 452 R-branch) were used to fit the upper state constants. The ν_9 band centre was found to be at 2324.359306 ± 0.000027 cm^{-1}. The ν_9 band centre derived from this work agrees closely with the calculated band centre value of 2326.98 cm^{-1} reported by J. L. Duncan in 1994 [37]. The rms value of 0.000428 cm^{-1} is close to the experimental uncertainty of ±0.00060 cm^{-1}. Thus, the spectral lines have been accurately fitted. The range of quantum numbers J', K_a' and K_c' of infrared transitions used in the

final fit is summarised in Table 5.2. The J' values ranges from 1-31, the K_a' values ranges from 0-14 while the K_c' values ranges from 0-22.

Table 5.2 *Quantum number ranges of infrared transitions used in the final fit*

Branch	J'	K_a'	K_c'	**No. or transitions fitted**
P	1-30	0-14	0-22	421
Q	1-31	0-12	0-21	408
R	2-31	0-14	0-21	452

A total of 1677 GSCDs from the infrared transitions of both the ν_{12} [24] and ν_9 bands of $^{13}C_2D_4$ were used to determine the final set of improved ground state constants. By using combination-differences to fit the ground state constants separately from the upper state constants, any perturbations of the upper state will not affect the ground state constants. The refined ground state constants obtained from this work are listed in Table 5.1, together with the ground state constants reported previously by T. L. Tan *et al.* [24]. Most of the ground state constants showed an improved accuracy. Compared to the previous work by T. L. Tan *et al.* [24] where 985 GSCDs were used in the fitting to get ground state constants, this study uses a more expanded set of GSCDs in the fit. In addition, both *A*-type transitions from the ν_{12} band and *B*-type transitions from the ν_9 band were used to compute the GSCDs, and this explains the greater accuracy of ground state constants.

CHAPTER 6

CONCLUDING REMARKS

6.1 Concluding Remarks

Ethylene is a plant hormone [4] and is a naturally occurring gas in planetary atmospheres of Jupiter [14], Saturn and Titan [17]. Due to the significance of ethylene gas in biological and atmospheric processes, spectroscopic research has been done on the unsubstituted ethylene molecule [18, 44] to have a better understanding of how the molecule rotates and vibrates. Various isotopes of ethylene have been studied [22, 38, 50] to understand how rotations and vibrations are affected by molecular mass. However, for the $^{13}C_2D_4$ molecule, only work on the ν_{12} band has been reported [24] and no work on the ν_9 band has been reported.

Recording of the infrared spectrum was carried out with the Bruker IFS 125 HR Michelson Fourier Transform Infrared (FTIR) Spectrophotometer, with an unapodised resolution of 0.0063 cm^{-1} in the frequency range of 2230 cm^{-1} to 2460 cm^{-1}. The spectrum was produced by coadding five runs of 200 scans each with total scanning of about 18 hours for all 1000 scans.

Calibration of the absorption lines of ν_9 band of $^{13}C_2D_4$ was carried out using unblended CO_2 lines in the range of 2298 cm^{-1} to 2377 cm^{-1}. In total, 38 CO_2 lines were fitted and the standard error of the fitted lines was found to be 0.0002 cm^{-1}. Accounting for systematic errors, the absolute uncertainty is approximated to be ± 0.0005 cm^{-1}.

In total, 1281 transitions were used in the fitting to get accurate upper state constants of the ν_9 band of $^{13}C_2D_4$. The fitting program used is based on Watson's A-reduced Hamiltonian in I^r representation [44, 45]. Rovibrational constants up to five quartic terms were obtained for the first time at high resolution. The ν_9 upper state constants were accurately derived to fit the observed transitions with a rms value of 0.000428 cm^{-1}. At the same time, 1677 GSCDs were used to refine the ground state constants of $^{13}C_2D_4$. The new infrared spectral data will lead to a better understanding of the molecular structure of the ethylene molecule.

6.2 Further Research

The investigations that have been conducted on the $^{13}C_2D_4$ molecule are limited to the ν_9 and ν_{12} bands. The ν_9 band is a *B*-type band, while the ν_{12} band is an *A*-type band and ideally, analysis of a *C*-type band of $^{13}C_2D_4$ should be carried out to improve the accuracy of the ground state constants. In addition, the vibrational bands of other isotopologues like $^{13}C_2H_4$ can be studied further to derive more accurate rotational constants. More accurate rotational constants will facilitate a better understanding of the molecular structure of ethylene and structural parameters like bond lengths and bond angles can be refined.

Besides, the research can be extended by studying the line intensities of individual spectral lines in the vibrational bands of ethylene and its isotopologues. The line intensity analysis reported so far are limited to the unsubstituted ethylene molecule, $^{12}C_2H_4$ [51] and the $^{13}C^{12}CH_4$ [50] isotopologue. Accurate prediction of line intensities is needed in the detection and quantification of ethylene gas concentration in unknown gas samples. Furthermore, knowledge of line intensities will lead to a greater understanding of molecular structure and molecular dipole moment.

REFERENCES

[1] B. Stuart, *Infrared Spectroscopy: Fundamentals and Applications*, John Wiley & Sons, Ltd, West Sussex (2004).

[2] F. B. Abeles, *Ethylene in Plant Biology*, Academic Press, New York (1973).

[3] C. Chang and A. B. Bleecker, *Plant Physiol.* **136** 2895-2899 (2004).

[4] S. F. Yang and N. E. Hoffman, *Ann. Rev. Plant Physiol.* **35** 155-189 (1984).

[5] F. B. Abeles and H. E. Heggestad, *J. Air Pollut. Control Ass.* **23** 517-521 (1973).

[6] T. Dudek, *Agriculture News,* Michigan State University, Michigan (2015).

[7] W. G. Doorn, *Annals of Botany* **89** 689-693 (2002).

[8] H. Mohr and P. Schopfer, *Plant Physiology*, Springer Verlag, Berlin (1995).

[9] H. Zimmermann and R. Walzl, *Ullmann's Encyclopedia of Industrial Chemistry*, Wiley Online Library (2009).

[10] J. Lazonby and D. Waddington, *The Essential Chemical Industry Online*, CIEC Promoting Science at the University of York, York (2015).

[11] J. G. Calvert, *Environ. Sci. Technol.*, **10** 256-262 (1976).

[12] C. N. Hewitt and A. Jackson, *Handbook of Atmospheric Science: Principles of Applications*, Blackwell Publishing, Malden (2003).

[13] H. Janin and S. A. Mandia, *Rising Sea Levels: An introduction to Cause and Impact*, McFarland & Company, North Carolina (2012).

[14] R. P. Wayne, *Chemistry of Atmospheres*, Oxford University Press, New York (1991).

[15] P. N. Romani, D. E. Jennings, G. L. Bjoraker, P. V. Sada, G. H. McCabe, R. J. Boyle, *Icarus* **198,** 420-434 (2008).

[16] B. Bezard, J. Moses, J. Lacy, T. Greathouse, M. Ritcher, C. Griffith, *Bull. Am. Astron. Soc.* **33,** 1079 (2001).

[17] D. J. Stevenson et al., *Science* **344,** 78-80 (2014).

[18] G.B. Lebron, T.L. Tan, *J. Mol. Spectrosc*. **283,** 29-31 (2013).

[19] G.B. Lebron, T.L. Tan, *J. Mol. Spectrosc*. **265,** 55-57 (2011).

[20] G.B. Lebron, T.L. Tan, *J. Mol. Spectrosc*. **271,** 44-49 (2012).

[21] T.L. Tan, M.G. Gabona, *J. Mol. Spectrosc*. **272,** 51-53 (2012).

[22] T.L. Tan, G.B. Lebron, *J. Mol. Spectrosc*. **269,** 109-112 (2011).

[23] T.L. Tan, M.G. Gabona, G.B. Lebron, *J. Mol. Spectrosc*. **266,** 113-115 (2011).

[24] T. L. Tan, M. G. Gabona, P. D. Godfrey, D. McNaughton, *J. Mol. Spectrosc.* **307,** 40-43 (2015).

[25] J. L. Duncan, D. C. McKean, and P. D. Mallinson, *J. Mol. Spectrosc*. **45,** 221-246 (1973).

[26] W. Gordy, W. V. Smith, and R. F. Trambarulo, *Microwave Spectroscopy*, John Wiley & Sons, Inc, New York (1953).

[27] D. Papousek and M. R. Aliev, *Molecular Vibrational-Rotational Spectra*, Elsevier, Amsterdam (1982).

[28] J. K. G. Watson, in "*Vibrational Spectra and Structure, A Series of Advances*" (J. R. Durig, Ed.), Vol. 6, Chap. 1, Elsevier, New York (1977).

[29] R. Georges, M. Bach, and M. Herman, *Mol. Phys*. **90,** 381-387 (1997).

[30] J. M. Hollas, *Basic atomic and molecular spectroscopy*, Wiley-Interscience, New York (2002).

[31] G. M. Barrow, *Introduction to Molecular Spectroscopy*, McGraw-Hill, USA (1962).

[32] K. Yamanouchi, *Quantum Mechanics of Molecular Structures*, Springer, London (2001).

[33] J. M. Hollas, *High Resolution Spectroscopy*, John Wiley & Sons, London (1998).

[34] C. N. Banwell, *Fundamentals of Molecular Spectroscopy*, McGraw-Hill, London (1983).

[35] O. N. Ulenikov et al, *J. Quant. Spectrosc. Radiat. Transf.* **118**, 14-25 (2013).

[36] P. F. Bernath, *Spectra of Atoms and Molecules*, Oxford University Press, New York (1995).

[37] J. L. Duncan, *Mol. Phys*. **83,** 159-169 (1994).

[38] M. G. Gabona, T. L. Tan, and J. Q. Woo, *J. Mol. Spectrosc.* **305**, 22-24 (2014).

[39] T. Oka and Y. Morino, *J. Mol. Spectrosc.* **6**, 472-482 (1961).

[40] P. Griffiths and J. A. Hasseth, *Fourier Transform Infrared Spectroscopy*, Wiley-Blackwell, New Jersey (2007).

[41] B. C. Smith, *Fundamentals of Fourier Transform Infrared Spectroscopy*, CRC Press LLC, Florida (1996).

[42] B. George and P. McIntyre, *Infrared Spectroscopy*, John Wiley & Sons, Ltd, England (1987).

[43] A. G. Maki, CALIB, unpublished, in.

[44] A. Maki, T. L. Tan, E. C. Looi, J. W. C Johns, M. Noel, *J. Mol. Spectrosc.*, **157,** 248-253 (1993).

[45] T. L. Tan, E. C. Looi, K. T. Kua, A. Maki, J. W. C. Johns, M. Noel, *J. Mol. Spectrosc.*, **149,** 425-434 (1991).

[46] G. Guelachvili and K. Narahari Rao, *Handbook of Infrared Standards*, Academic Press, Orlando, FL (1986).

[47] D. McNaughton, D. McGilvery and F. Shankes, J. Mol. Spectrosc. **149,** 458-473 (1991).

[48] J. K. G. Watson, *J. Chem. Phys.* **46**, 1935-1949 (1967).

[49] G. B. Lebron, T. L. Tan, *J. Mol. Spectrosc.* **288,** 11-13 (2013).

[50] J. M. Flaud, W. J. Lafferty, V. Malathy Devi, R. L. Sams, D. Chris Benner, *J. Mol. Spectrosc.* **267,** 3-12 (2011).

[51] G. B. Lebron and T. L. Tan, Int. J. Spectrosc. **2013**, 7 (2013).